CORONAVIRUS

An orally bioavailable broad-spectrum antiviral inhibits SARS-CoV-2 in human airway epithelial cell cultures and multiple coronaviruses in mice

Timothy P. Sheahan[1]*†, Amy C. Sims[1]*‡, Shuntai Zhou[2], Rachel L. Graham[1], Andrea J. Pruijssers[3], Maria L. Agostini[3], Sarah R. Leist[1], Alexandra Schäfer[1], Kenneth H. Dinnon III[1,4], Laura J. Stevens[3], James D. Chappell[3], Xiaotao Lu[3], Tia M. Hughes[3], Amelia S. George[3], Collin S. Hill[2], Stephanie A. Montgomery[5], Ariane J. Brown[1], Gregory R. Bluemling[6,7], Michael G. Natchus[6], Manohar Saindane[6], Alexander A. Kolykhalov[6,7], George Painter[6,7,8], Jennifer Harcourt[9], Azaibi Tamin[9], Natalie J. Thornburg[9], Ronald Swanstrom[2,10], Mark R. Denison[3], Ralph S. Baric[1,4†]

Coronaviruses (CoVs) traffic frequently between species resulting in novel disease outbreaks, most recently exemplified by the newly emerged SARS-CoV-2, the causative agent of COVID-19. Here, we show that the ribonucleoside analog β-D-N^4-hydroxycytidine (NHC; EIDD-1931) has broad-spectrum antiviral activity against SARS-CoV-2, MERS-CoV, SARS-CoV, and related zoonotic group 2b or 2c bat-CoVs, as well as increased potency against a CoV bearing resistance mutations to the nucleoside analog inhibitor remdesivir. In mice infected with SARS-CoV or MERS-CoV, both prophylactic and therapeutic administration of EIDD-2801, an orally bioavailable NHC prodrug (β-D-N^4-hydroxycytidine-5′-isopropyl ester), improved pulmonary function and reduced virus titer and body weight loss. Decreased MERS-CoV yields in vitro and in vivo were associated with increased transition mutation frequency in viral, but not host cell RNA, supporting a mechanism of lethal mutagenesis in CoV. The potency of NHC/EIDD-2801 against multiple CoVs and oral bioavailability highlights its potential utility as an effective antiviral against SARS-CoV-2 and other future zoonotic CoVs.

INTRODUCTION

The genetically diverse Orthocoronavirinae [coronavirus (CoV)] family circulates in many avian and mammalian species. Phylogenetically, CoVs are divided into four genera: alpha (group 1), beta (group 2), gamma (group 3), and delta (group 4). Three new human CoV have emerged in the past 20 years with severe acute respiratory syndrome CoV (SARS-CoV) in 2002, Middle East respiratory syndrome CoV (MERS-CoV) in 2012, and now SARS-CoV-2 in 2019 (*1*–*3*). All human CoV are thought to have emerged originally as zoonoses (*4*–*6*). The ongoing SARS-CoV-2 pandemic [referred to as CoV disease 2019 (COVID-19)] has caused more than 500,000 infections and more than 25,000 deaths in 199 countries. Like SARS-CoV and MERS-CoV, the respiratory disease caused by SARS-CoV-2 can progress to acute lung injury (ALI), an end-stage lung disease with limited treatment options and very poor prognoses (*3*, *7*, *8*). This emergence paradigm is not limited to humans. A novel group 1 CoV called swine acute diarrhea syndrome CoV (SADS-CoV) recently emerged from bats causing the loss of more than 20,000 pigs in Guangdong Province, China (*9*). More alarmingly, many group 2 SARS-like and MERS-like CoVs are circulating in bat reservoir species that can use human receptors and replicate efficiently in primary human lung cells without adaptation (*9*–*12*). The presence of these "preepidemic" zoonotic strains foreshadow the emergence and epidemic potential of additional SARS-like and MERS-like viruses in the future. Given the diversity of CoV strains in zoonotic reservoirs and a penchant for emergence, broadly active antivirals are clearly needed for rapid response to new CoV outbreaks in humans and domesticated animals.

Currently, there are no approved therapies specific for any human CoV. β-D-N^4-hydroxycytidine (NHC; EIDD-1931) is an orally bioavailable ribonucleoside analog with broad-spectrum antiviral activity against various unrelated RNA viruses including influenza, Ebola, CoV, and Venezuelan equine encephalitis virus (VEEV) (*13*–*16*). For VEEV, the mechanism of action (MOA) for NHC has been shown to be through lethal mutagenesis where deleterious transition mutations accumulate in viral RNA (*14*, *17*). Thus, we sought to determine NHC's breadth of antiviral activity against multiple emerging CoV, its MOA for CoV, and its efficacy in mouse models of CoV pathogenesis.

RESULTS

NHC potently inhibits MERS-CoV and newly emerging SARS-CoV-2 replication

To determine whether NHC blocks the replication of highly pathogenic human CoV, we performed antiviral assays in cell lines with MERS-CoV and the newly emerging SARS-CoV-2. We first assessed the antiviral activity of NHC against MERS-CoV in the human lung

[1]Department of Epidemiology, University of North Carolina at Chapel Hill, Chapel Hill, NC 27599, USA. [2]Lineberger Comprehensive Cancer Center, University of North Carolina at Chapel Hill, Chapel Hill, NC 27599, USA. [3]Department of Pediatrics, Vanderbilt University Medical Center, Nashville, TN 37232, USA. [4]Department of Microbiology and Immunology, University of North Carolina at Chapel Hill, Chapel Hill, NC 27599, USA. [5]Department of Pathology and Laboratory Medicine, University of North Carolina, Chapel Hill, NC 27599, USA. [6]Emory Institute of Drug Development (EIDD), Emory University, Atlanta, GA 30322, USA. [7]Drug Innovation Ventures at Emory (DRIVE), Atlanta, GA 30322, USA. [8]Department of Pharmacology and Chemical Biology, Emory University, Atlanta, GA 30322, USA. [9]Division of Viral Diseases, Centers for Disease Control and Prevention, Atlanta, GA 30329, USA. [10]Department of Biochemistry and Biophysics, University of North Carolina at Chapel Hill, Chapel Hill, NC 27599, USA.
*These authors contributed equally to this work.
†Corresponding author. Email: sheahan@email.unc.edu (T.P.S.); rbaric@email.unc.edu (R.S.B.)
‡Present address: National Security Division, Pacific Northwest National Laboratory, Chemical and Biological Signature Sciences, Richland, WA 99352, USA.

epithelial cell line Calu-3 2B4 ("Calu-3" cells). Using a recombinant MERS-CoV expressing nanoluciferase (MERS-nLUC) (*18*), we measured virus replication in cultures exposed to a dose range of drug for 48 hours. NHC was potently antiviral with an average median inhibitory concentration (IC_{50}) of 0.15 μM and no observed cytoxicity in similarly treated uninfected cultures across the dose range [50% cytotoxic concentration (CC_{50}) of >10 μM; Fig. 1A]. The therapeutic index for NHC was >100. Using a clinical isolate of SARS-CoV-2 (2019-nCoV/USA-WA1/2020), we performed antiviral assays in African green monkey kidney (Vero) cells and found that NHC was potently antiviral with an IC_{50} of 0.3 μM and CC_{50} of >10 μM (Fig. 1B). We then determined the antiviral activity of NHC against SARS-CoV-2 in the Calu-3 cells through the measurement of infectious virus production and viral genomes. We observed a dose-dependent reduction in virus titers (Fig. 1C) with an IC_{50} of 0.08 μM. Viral genomic RNA was quantitated in clarified supernatants by quantitative reverse transcription polymerase chain reaction (qRT-PCR; Fig. 1D). Like the effect on infectious titers, we found a dose-dependent reduction in viral genomic RNA and a similar calculated IC_{50} of 0.09 μM. Collectively, these data demonstrate that NHC is potently antiviral against two genetically distinct emerging CoV.

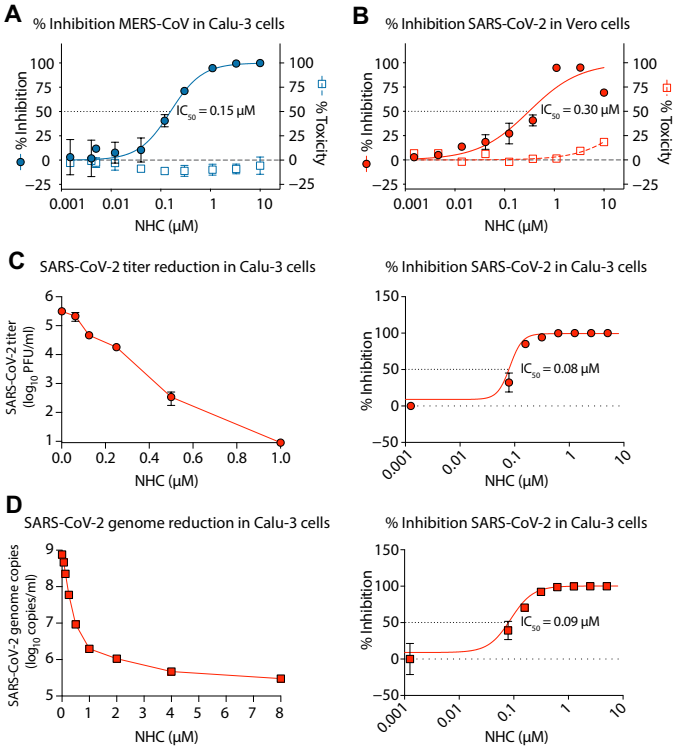

Fig. 1. NHC potently inhibits MERS-CoV and newly emerging SARS-CoV-2 replication. (**A**) Percent inhibition of MERS-CoV replication and NHC cytotoxicity in Calu-3 cells. Calu-3 cells were infected in triplicate with MERS-CoV nanoluciferase (MERS-nLUC) at a multiplicity of infection (MOI) of 0.08 in the presence of a range of drug for 48 hours, after which replication was measured through quantitation of MERS-CoV–expressed nLUC. Cytotoxicity was measured in similarly treated but uninfected cultures via CellTiter-Glo assay. Data are combined from three independent experiments. (**B**) NHC antiviral activity and cytotoxicity in Vero E6 cells infected with SARS-CoV-2. Vero E6 cells were infected in duplicate with SARS-CoV-2 clinical isolate 2019-nCoV/USA-WA1/2020 virus at an MOI of 0.05 in the presence of a range of drug for 48 hours, after which replication was measured through quantitation of cell viability by CellTiter-Glo assay. Cytotoxicity was measured as in (A). Data are combined from two independent experiments. (**C**) SARS-CoV-2 titer reduction (left) and percent inhibition (right) in Calu-3 cells. Cells were infected with SARS-CoV-2 at an MOI of 0.1 for 30 min, washed, and exposed to a dose response of NHC in triplicate per condition. At 72 hpi, virus production was measured by plaque assay. (**D**) SARS-CoV-2 genomic RNA reduction (left) and percent inhibition (right) in Calu-3 cells. Viral RNA was isolated from clarified supernatants from the study in (C). Genome copy numbers were quantitated by qRT-PCR with primer/probes targeting the N gene. For (A) to (D), the symbol is at the mean, and the error bars represent the SD.

NHC is highly active against SARS-CoV-2, MERS-CoV, and SARS-CoV in primary human airway epithelial cell cultures

To determine whether NHC would be similarly antiviral in primary human cells, we performed a series of studies in primary human airway epithelia (HAE) cell cultures. HAE models the architecture and cellular complexity of the conducting airway and is readily infected by multiple human and zoonotic CoV, including SARS-CoV and MERS-CoV (*19*). We first assessed the cytotoxicity of NHC in HAE treated with an extended dose range for 48 hours using quantitative PCR of cell death–related gene transcripts as our metric. NHC treatment did not appreciably alter gene expression even at doses up to 100 μM (fig. S1). We then sought to determine whether NHC would inhibit clinical isolate SARS-CoV-2 replication in HAE. We observed a dose-dependent reduction in SARS-CoV-2 infectious virus production (Fig. 2A). In MERS-CoV–infected HAE, NHC substantially reduced virus production with maximal titer reduction of >5 logs at 10 μM (average IC_{50} = 0.024 μM), which correlated with reduced genomic open reading frame 1 (ORF1) and subgenomic [ORF nucleocapsid (ORFN)] RNA in paired samples (Fig. 2B). We observed similar trends in titer reduction (>3 log at 10 μM, average IC_{50} = 0.14 μM) and in copies of genomic and subgenomic RNA in SARS-CoV–infected HAE (Fig. 2C). Thus, NHC was potently antiviral against SARS-CoV-2, MERS-CoV, and SARS-CoV in primary human epithelial cell cultures without cytotoxicity.

NHC is effective against remdesivir-resistant virus and multiple distinct zoonotic CoV

CoV are taxonomically divided into multiple genogroups (alpha, beta, gamma, and delta), but human-infecting CoV are found only in the alpha and beta subgroups thus far (Fig. 3A). There is high sequence conservation in the RNA-dependent RNA polymerase [RdRp; nonstructural protein 12 (nsp12)] across CoV (Fig. 3A). For example, the RdRp of SARS-CoV-2 has 99.1% similarity and 96% amino acid identity to that of SARS-CoV (Fig. 3A). To gain insight into structural conservation of RdRp across the CoV family, we modeled the variation reflected in the RdRp dendrogram in Fig. 3A onto the structure of the SARS-CoV RdRp (Fig. 3B) (*20*). The core of the RdRp molecule and main structural motifs that all RdRp harbor (Fig. 3B and fig. S2) is highly conserved among CoV including SARS-CoV-2. We previously reported that CoV resistance to another broad-spectrum nucleoside analog, remdesivir (RDV), was mediated by RdRp residues F480L and V557L in a model CoV mouse hepatitis virus (MHV) and in SARS-CoV, resulting in a fivefold shift in IC_{50} (Fig. 3C) (*21*). Consequently, we tested whether RDV resistance mutations in MHV conferred cross-resistance to NHC. The two RDV resistance mutations, alone or together, conferred increased sensitivity to inhibition by NHC (Fig. 3D). As our previous studies have demonstrated a high genetic barrier to NHC for VEEV, influenza, and CoV (*14*–*16*), the lack of cross-resistance further suggests that

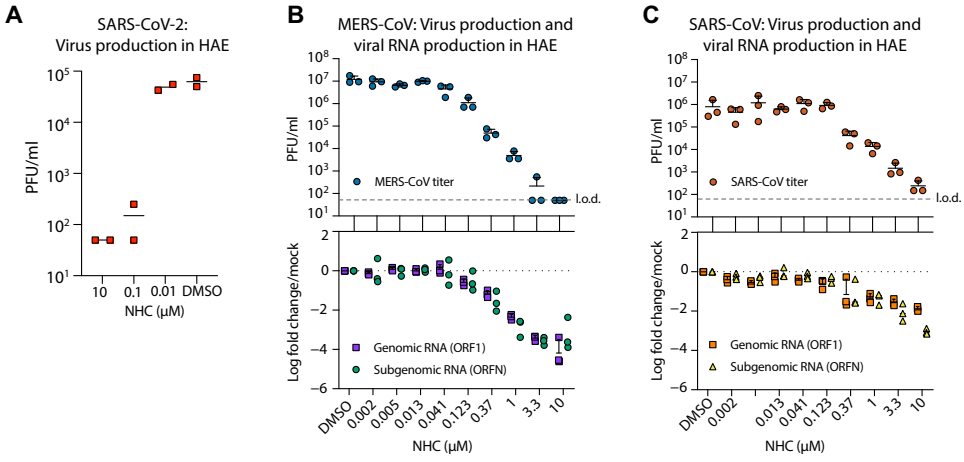

Fig. 2. NHC is highly active against SARS-CoV-2, MERS-CoV, and SARS-CoV in primary HAE cell cultures. (**A**) Human airway epithelia (HAE) cultures were infected at an MOI of 0.5 with clinical isolate SARS-CoV-2 for 2 hours in the presence of NHC in duplicate, after which the virus was removed, and cultures were washed in, incubated in NHC for 48 hours when apical washes were collected for virus titration by plaque assay. The line is at the mean. Each symbol represents the titer from a single well. (**B**) HAE cells were infected with MERS-CoV red fluorescent protein (RFP) at an MOI of 0.5 in triplicate and treated similarly to (A). qRT-PCR for MERS-CoV ORF1 and ORFN mRNA. Total RNA was isolated from cultures in (**C**) for qRT-PCR analysis. Representative data from three separate experiments with three different cell donors are displayed. PFU, plaque-forming units; l.o.d., limit of detection. (C) Studies performed as in (A) but with SARS-CoV green fluorescent protein (GFP). Representative data from two separate experiments with two different cell donors are displayed. Each symbol represents the data from one HAE culture, the line is at the mean, and the error bars represent the SD.

NHC and RDV may select for exclusive and mutually sensitizing resistance pathways.

To explore the breadth of antiviral efficacy against zoonotic CoV, we performed antiviral assays in HAE with three zoonotic bat-CoV: SHC014, HKU3, and HKU5. Closely related to the beta 2b SARS-CoV, bat-CoV SHC014 is capable of replicating human cells without adaptation (*11*), suggesting its potential for zoonotic emergence into humans. The more distantly related SARS-like beta 2b CoV, recombinant bat-CoV HKU3, has a modified receptor-binding domain to facilitate growth in cell culture (*22*). Last, bat-CoV HKU5 is a MERS-like beta 2c CoV (*23*). NHC diminished infectious virus production and the levels of genomic/subgenomic viral RNA in HAE in a dose-dependent manner for all three bat-CoVs (Fig. 4). Therefore, the antiviral activity of NHC was not limited by natural amino acid variation in the RdRp, which, among the group 2b and group 2c CoV, can vary by almost 20%. Moreover, these data suggest that if another SARS- or MERS-like virus was to spill over into humans in the future, they would likely be susceptible to the antiviral activity of NHC.

NHC antiviral activity is associated with increased viral mutation rates

It has recently been shown that NHC treatment increases the mutation rate in viral genomic RNA of Rous sarcoma virus (*24*), VEEV (*14*), and influenza (*24*), and our previous study used RNA sequencing (RNA-seq) to show that overall transition mutation frequency is increased during NHC treatment of MHV and MERS-CoV during infection in continuous cell lines (*16*). We sought to determine whether NHC would increase the mutation frequency during MERS-CoV infection in human primary HAE. Using MERS-CoV–infected HAE treated with either vehicle or a dose range of NHC or RDV, we show that both drugs reduced virus titers in a dose-dependent manner (Fig. 5A). We then used a highly sensitive, high-fidelity deep-sequencing approach [Primer ID next-generation sequencing (NGS)], which uses barcoded degenerate primers and Illumina-indexed libraries to determine accurate mutation rates on viral RNA production (*25*). Using this approach, we analyzed a 538–base pair (bp) region of viral genomic RNA in nsp15. The error rates (number of mutations per 10,000 bases) in vehicle-treated (0.01) or RDV-treated (0.01) cultures were very low. RDV is reported to act via chain termination of nascent viral RNA, and thus, the low error rates in RDV-treated cultures are in line with the proposed MOA (*26*). In contrast, the error rate was significantly increased in NHC-treated MERS-CoV RNA in a dose-dependent manner {two-way analysis of variance (ANOVA) with Dunnett's multiple comparison test; 10-fold increase at 10 μM [$P < 0.0001$ at 24 and 48 hours post-infection (hpi)] and fivefold increase at 1 μM ($P < 0.0001$ at 24 hpi and $P = 0.0015$ at 48 hpi; Fig. 5C}. The magnitude of the error rate in NHC-treated cultures correlated with virus titer reduction. At 48 hpi, the respective error rate and virus titer was 0.015×10^6 and 3.96×10^6 plaque-forming units (PFU)/ml for vehicle treatment, 0.045×10^4 and 2.86×10^4 PFU/ml with 1 μM NHC, and 0.090×10^2 and 1.5×10^2 PFU/ml with 10 μM NHC. Thus, with 1 μM NHC, a threefold increase in error rate resulted in a 138-fold decrease in virus titer, whereas with 10 μM NHC, a sixfold increase in error rate resulted in a 26,000-fold decrease in virus titer.

We then examined the mutational spectra induced by NHC, which can be incorporated into viral RNA as a substitution for either cytosine (C) or uracil (U). RNA-mutagenic antivirals may incorporate in both nascent negative- and positive-sense RNA during genome replication (Fig. 5D). Adenine-to-guanine (A-to-G) and U-to-C transitions were enriched in MERS-CoV genomic RNA in an NHC dose-dependent manner (Fig. 5E). Collectively, these data used high-fidelity sequence analysis to demonstrate a specific enrichment for A:G and C:U transitions in MERS-CoV RNA after NHC treatment of primary HAE cell cultures.

Therapeutic EIDD-2801 reduces SARS-CoV replication and pathogenesis

Given the promising antiviral activity of NHC in vitro, we next evaluated its in vivo efficacy using EIDD-2801, an orally bioavailable prodrug of NHC (β-D-N^4-hydroxycytidine-5′-isopropyl ester), designed for improved in vivo pharmacokinetics and oral bioavailability in humans and nonhuman primates (*15*). The plasma profiles of NHC and EIDD-2801 are similar in mice after oral delivery (*15*). We first performed a prophylactic dose escalation study in C57BL/6 mice where we orally administered vehicle [10% polyethylene glycol (PEG) and 2.5% Cremophor RH 40 in water] or EIDD-2801 (50, 150, or 500 mg/kg) 2 hours before intranasal infection with 5×10^4 PFU of mouse-adapted SARS-CoV (SARS-MA15) and then vehicle or drug every 12 hours thereafter. Beginning at 3 days post-infection (dpi) and through the end of the study, body weight

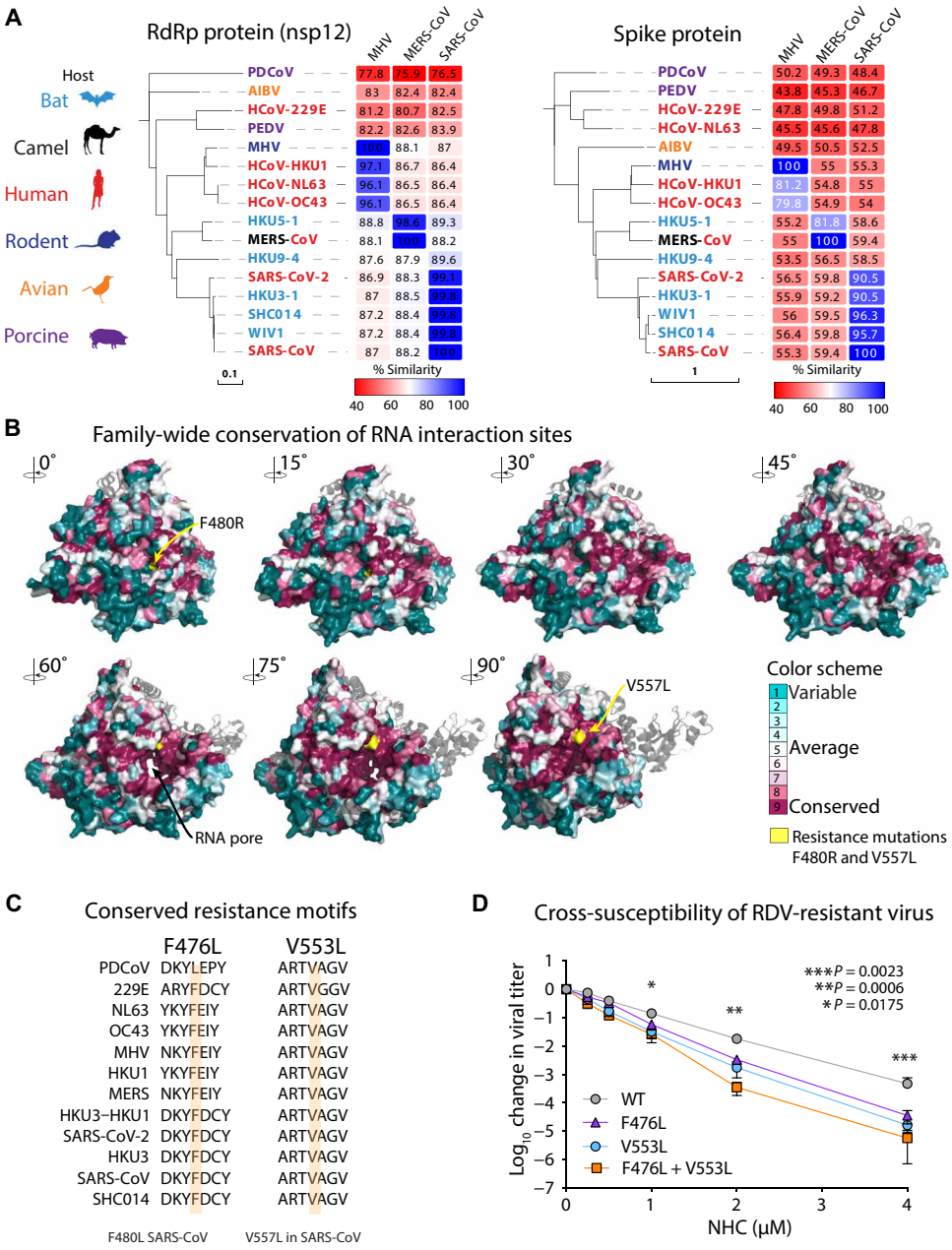

Fig. 3. Remdesivir resistance mutations in the highly conserved RdRp increase susceptibility to NHC. (**A**) Neighbor-joining trees created with representatives from all four CoV genogroups showing the genetic similarity of CoV nsp12 (RdRp) and CoV spike glycoprotein, which mediates host tropism and entry into cells. Text color of the virus strain label corresponds to virus host species on the left. The heat map adjacent to each neighbor-joining tree depicts percent amino acid identity (% amino acid similarity) against mouse hepatitis virus (MHV), SARS-CoV, or MERS-CoV. (**B**) The variation encompassed in (A) was modeled onto the RdRp structure of the SARS-CoV RdRp. (**C**) Amino acid sequence of CoV in (A) at known resistance alleles to antiviral drug remdesivir (RDV). (**D**) Virus titer reduction assay in DBT cells across a range of NHC with recombinant MHV bearing resistance mutations to RDV. Data shown are combined from three independent experiments performed with biological duplicates or triplicates per condition. Asterisks indicate statistically significant differences by Mann-Whitney test as indicated on the graph.

loss compared to vehicle treatment was significantly diminished (50 mg/kg) or prevented (150 and 500 mg/kg) with EIDD-2801 prophylaxis (two-way ANOVA with Dunnett's multiple comparison test, $P < 0.0001$; fig. S3A). Lung hemorrhage was also significantly reduced 5 dpi with EIDD-2801 (500 mg/kg) treatment (Kruskal-Wallis test, $P = 0.010$; fig. S3B). There was a dose-dependent reduction in SARS-CoV lung titer (median titers: 50 mg/kg = 7×10^3 PFU/ml, 150 mg/kg = 2.5×10^3 PFU/ml, 500 mg/kg = 50 PFU/ml, and vehicle = 6.5×10^4 PFU/ml) with significant differences (Kruskal-Wallis with Dunn's multiple comparisons test) among the vehicle, 150 mg/kg ($P = 0.03$), and 500 mg/kg ($P = 0.006$) groups. Thus, prophylactic orally administered EIDD-2801 was robustly antiviral and able to prevent SARS-CoV replication and disease.

Since only the 500 mg/kg group significantly diminished weight loss, hemorrhage, and reduced lung titer to near undetectable levels, we tested this dose under therapeutic treatment conditions to determine

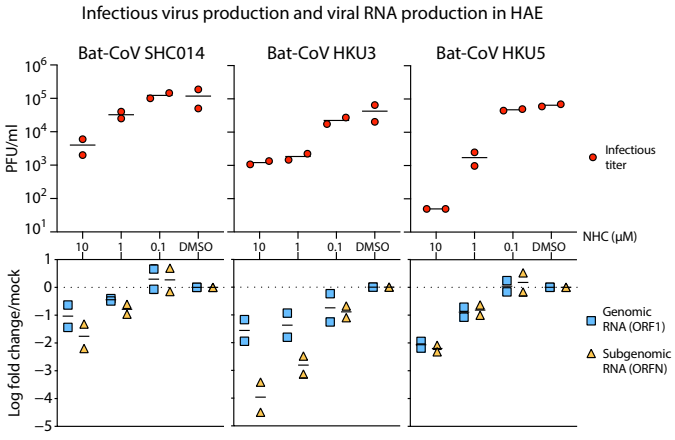

Fig. 4. NHC is effective against multiple genetically distinct bat-CoV. (**Top**) Antiviral efficacy of NHC in HAE cells against SARS-like (HKU3 and SHC014, group 2b) and MERS-like (HKU5, group 2c) bat-CoV. HAE cells were infected at an MOI of 0.5 in the presence of NHC in duplicate. After 48 hours, the virus produced was titrated via plaque assay. Each data point represents the titer per culture. (**Bottom**) qRT-PCR for CoV ORF1 and ORFN mRNA in total RNA from cultures in the top panel. Mock, mock treated. Representative data from two separate experiments with two different cell donors are displayed.

whether EIDD-2801 could improve the outcomes of an ongoing CoV infection. As a control, we initiated oral vehicle or EIDD-2801 2 hours before infection with 1×10^4 PFU SARS-MA15. For therapeutic conditions, we initiated EIDD-2801 treatment at 12, 24, or 48 hpi. After initiating treatment, dosing for all groups was performed every 12 hours for the duration of the study. Both prophylactic treatment initiated 2 hours before infection and therapeutic treatment initiated 12 hpi significantly (two-way ANOVA with Tukey's multiple comparison test) prevented body weight loss after SARS-CoV infection on 2 dpi and thereafter (−2 hours, $P = 0.0002$ to <0.0001; +12 hours, $P = 0.0289$ to <0.0001) as compared to vehicle-treated animals (Fig. 6A). Treatment initiated 24 hpi also significantly reduced body weight loss (3 to 5 dpi, $P = 0.01$ to <0.0001), although not to the same degree as the earlier treatment initiation groups. When initiated 48 hpi, body weight loss was only different from vehicle on 4 dpi ($P = 0.037$; Fig. 6A). Therapeutic EIDD-2801 significantly (Kruskal-Wallis with Dunnett's multiple comparison test) reduced lung hemorrhage when initiated up to 24 hpi (−2, +12, and + 24 hours, $P < 0.0001$), mirroring the body weight loss phenotypes (Fig. 6B). All EIDD-2801–treated mice had significantly (Kruskal-Wallis with Dunnett's multiple comparison test) reduced viral loads in the lungs even in the +48-hour group (All $P < 0.0001$; Fig. 6C), which experienced the least protection from body weight loss and lung hemorrhage. We also measured pulmonary function via whole-body plethysmography (WBP). In Fig. 6D, we show that the WBP enhanced pause (PenH) metric, which is a surrogate marker for bronchoconstriction or pulmonary obstruction (*27*), was significantly (two-way ANOVA with Dunnett's multiple comparison test) improved throughout the course of the study if treatment was initiated up to 12 hpi [−2 hours, $P < 0.0001$ to 0.019 (2 to 5 dpi); +12 hours, $P < 0.0001$ to 0.0192 (2 to 5 dpi)], although the +24-hour group showed sporadic improvement as well (3 dpi, $P = 0.002$; Fig. 6D). Last, we blindly evaluated hematoxylin and eosin–stained lung tissue sections for histological features of ALI using two different and complementary scoring tools (*18*), which show that treatment initiated up to +12 hours significantly reduced ALI [Kruskal-Wallis with Dunn's multiple comparison test; American Thoracic Society lung injury score: −2 hours, $P = 0.0004$; +12 hours, $P = 0.0053$; diffuse alveolar damage (DAD) score: −2 hours, $P = 0.0015$; +12 hours, $P = 0.0004$; Fig. 6E]. Together, therapeutic EIDD-2801 was potently antiviral against SARS-CoV in vivo, but the degree of clinical benefit was dependent on the time of initiation after infection.

EIDD-2801 prophylactic and therapeutic efficacy correlates with increased MERS-CoV mutation rate

After obtaining promising in vivo efficacy data with SARS-CoV, we investigated whether EIDD-2801 would be effective against MERS-CoV. Because the murine ortholog of the MERS-CoV receptor, dipeptidyl peptidase 4 (DPP4), does not support viral binding and entry, all in vivo studies were performed in genetically modified mice encoding a murine DPP4 receptor encoding two human residues at positions 288 and 330 [humanized DPP4 (hDPP4) 288/330 mice] (*18*, *28*). Similar to our SARS-CoV data, all doses of prophylactic EIDD-2801 (50, 150, and 500 mg/kg) protected hDPP4 288/330 mice (fig. S4) from significant body weight loss (two-way ANOVA with Dunnett's multiple comparison test, $P = 0.03$ to <0.0001), lung hemorrhage (Kruskal-Wallis with Dunn's multiple comparison test, $P = 0.01$ to <0.0001), and virus replication, which was undetectable (Kruskal-Wallis with Dunn's multiple comparison test, $P < 0.0001$) regardless of drug dose after intranasal infection with 5×10^4 PFU mouse-adapted MERS-CoV (fig. S4).

We then evaluated the therapeutic efficacy EIDD-2801 after the promising results of our prophylactic studies. Similar to our SARS-CoV study, EIDD-2801 treatment administered before or 12 hours after intranasal mouse-adapted MERS-CoV infection (5×10^4 PFU) prevented body weight loss from 2 to 6 dpi (two-way ANOVA with Tukey's multiple comparison test, $P = 0.02$ to <0.0001; Fig. 7A) and lung hemorrhage on 6 dpi (Kruskal-Wallis with Dunn's multiple comparison test, $P = 0.0004$ to <0.0001; Fig. 7B), but treatment initiated 24 or 48 hours did not offer similar protection. Unlike body weight loss and lung hemorrhage data, which varied by treatment initiation time, virus lung titer on 6 dpi was significantly reduced to the limit of detection in all treatment groups (Kruskal-Wallis with Dunn's multiple comparison test, $P < 0.0001$; Fig. 7C). When viral genomic RNA was quantified in paired samples of lung tissue, EIDD-2801 significantly reduced quantities of viral RNA (one-way ANOVA with Dunnett's multiple comparison test, $P < 0.0001$ to 0.017) in an initiation time-dependent manner for all groups except for +48 hours (Fig. 7D). The discrepancy among infectious titers and viral RNA suggests that accumulated mutations render the particles noninfectious and undetectable by plaque assay, consistent with the MOA. To gauge the effect of EIDD-2801 treatment on lung function, we assessed pulmonary function by WBP. Mirroring the body weight loss data, normal pulmonary function was only observed in groups where treatment was initiated before or 12 hpi [two-way ANOVA with Tukey's multiple comparison test, −2 hours, $P < 0.0001$ (3 dpi) and $P = 0.0002$ (4 dpi); +12 hours, $P < 0.0001$ (3 dpi) and $P = 0.0008$ (4 dpi); Fig. 7E]. Collectively, these data demonstrate that NHC prodrug, EIDD-2801, robustly reduces MERS-CoV infectious titers, viral RNA, and pathogenesis under both prophylactic and early therapeutic conditions.

To study the molecular mechanisms associated with drug performance in vivo, we investigated the correlation between infectious virus production and EIDD-2801–mediated mutagenesis of

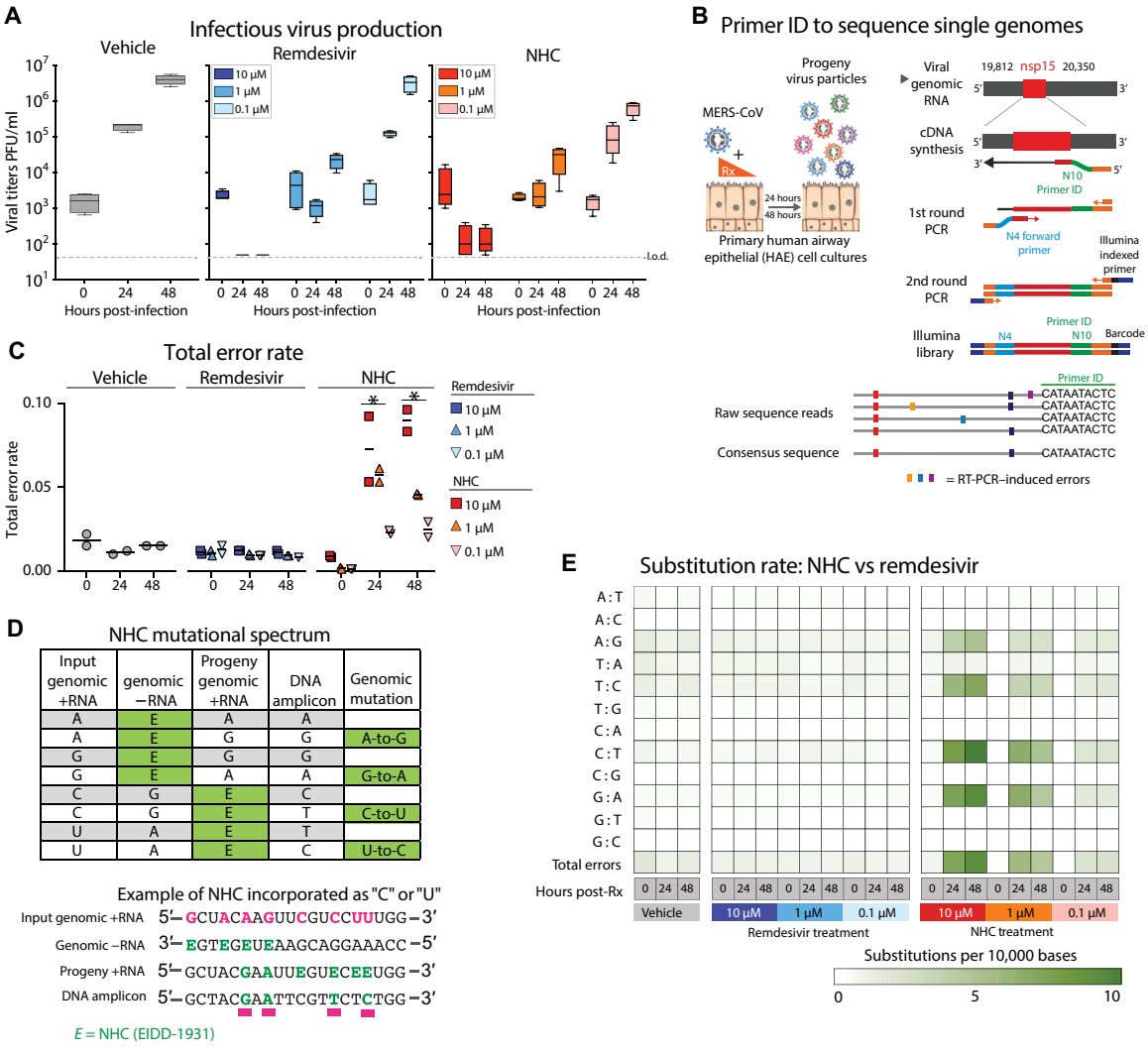

Fig. 5. NHC antiviral activity is associated with increased viral mutation rates. (**A**) HAE cultures were infected with MERS-CoV red fluorescent protein (RFP) at an MOI of 0.5 in duplicate in the presence of vehicle, RDV, or NHC for 48 hours, after which apical washes were collected for virus titration. Data are combined from two independent studies. The boxes encompass the 25th to 75th percentile, the line is at the median, and the whiskers represent the range. (**B**) Schematic of Primer ID deep sequencing for single RNA genomes of MERS-CoV. (**C**) The total error rate for MERS-CoV RNA isolated from cultures in (A) as determined by Primer ID. Error rate values are number of mutations per 10,000 bases. Asterisk indicates significant differences as compared to untreated group by two-way ANOVA with a Dunnett's multiple comparison test. (**D**) Description of potential NHC mutational spectra on both positive- and negative-sense viral RNA. (**E**) Nucleotide transitions in cDNA were derived from MERS-CoV genomic RNA.

MERS-CoV RNA under therapeutic treatment conditions. Using Primer ID NGS, we measured the mutation rates of both viral genomic RNA (nsp10) and host interferon-stimulated gene 15 (*ISG15*) mRNA, a highly up-regulated innate immune-related gene after MERS-CoV infection (Fig. 7F). Primer ID NGS measures the mutational frequency in single RNA molecules, each of which is represented by a single template consensus sequence (TCS) (*25*). Viral TCS were significantly reduced (two-way ANOVA with Tukey's multiple comparison test, −2 hours, $P < 0.0001$; +12 hours, $P = 0.0001$; and +24 hours, $P = 0.02$) in a treatment initiation time-dependent manner (Fig. 7G) similar to viral genomic RNA measured by qRT-PCR. In contrast, the numbers of ISG15 TCS were similar ($P = 0.2$ to 0.8) for all groups, indicating that neither vehicle nor drug treatment significantly affected the levels of or mutated ISG15 mRNA transcripts (Fig. 7G). Similar to our TCS data in Fig. 6G, the total error rate in viral nsp10 was significantly increased (two-way ANOVA with Tukey's multiple comparison test) in groups where treatment was initiated before (−2 hours, median error rate = 10.5 errors per 10,000 bases, $P < 0.0001$) and up to 24 hpi (12 hours, median error rate = 8.2 errors per 10,000 bases, $P < 0.0001$; +24 hours, median error rate = 5.4 errors per 10,000 bases, $P = 0.0003$), but the error rates in ISG15 remained at baseline for all groups (Fig. 7H). In addition, nucleotide transitions observed in MERS-CoV genomes in vitro were also observed in vivo in groups where treatment was initiated before and up to 12 hpi (two-way ANOVA with Tukey's multiple comparison test, $P = 0.0003$ to <0.0001; Fig. 7I). These transitions were not observed in host ISG15 mRNA (Fig. 7I). Last, the EIDD-2801 dose-dependent mutagenesis of viral RNA correlated with an increase in codon change frequency, including stop codons, in mice where treatment was initiated 12 hours or before (two-way ANOVA with

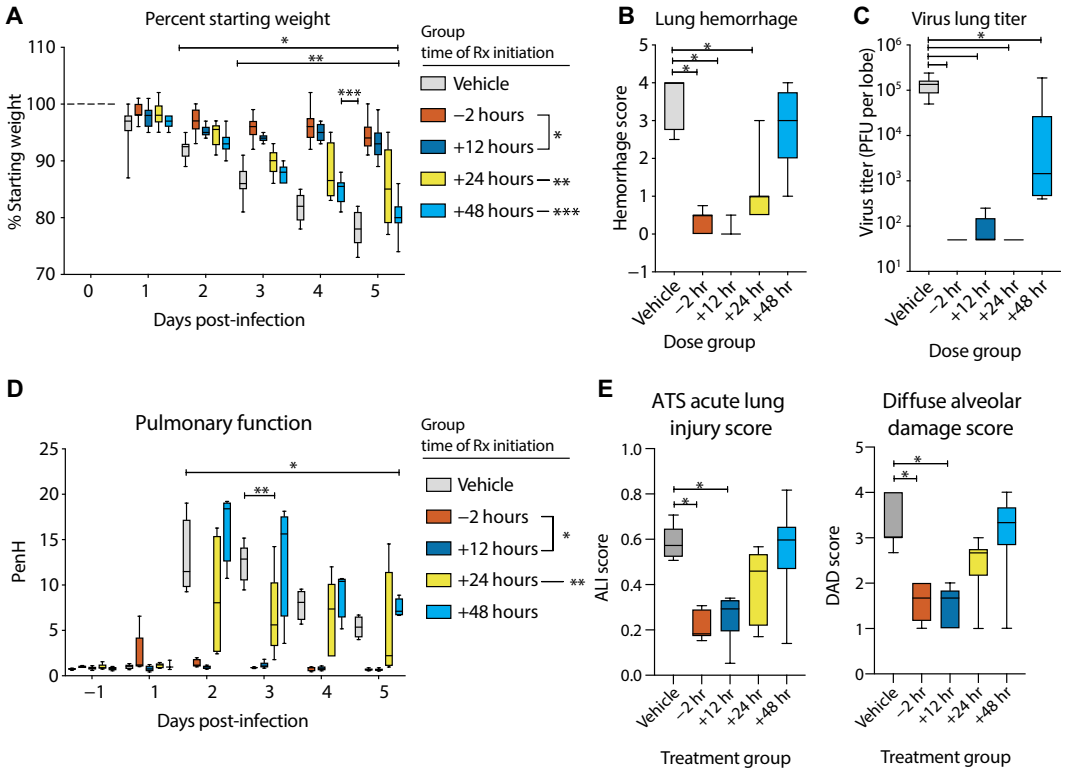

Fig. 6. Prophylactic and therapeutic EIDD-2801 reduces SARS-CoV replication and pathogenesis. Equivalent numbers of 25- to 29-week-old male and female C57BL/6 mice were administered vehicle (10% PEG and 2.5% Cremophor RH 40 in water) or NHC prodrug EIDD-2801 beginning at −2, +12, +24, or + 48 hpi and every 12 hours thereafter by oral gavage ($n = 10$ per group). Mice were intranasally infected with 1×10^4 PFU mouse-adapted SARS-CoV MA15 strain. (**A**) Percent starting weight. Asterisks indicate differences from vehicle treated by two-way ANOVA with Tukey's multiple comparison test. (**B**) Lung hemorrhage in mice from (A) scored on a scale of 0 to 4, where 0 is a normal pink healthy lung and 4 is a diffusely discolored dark red lung. (**C**) Virus lung titer in mice from (A) as determined by plaque assay. Asterisks in both (B) and (C) indicate differences from vehicle by one-way ANOVA with a Dunnett's multiple comparison test. (**D**) Pulmonary function by whole-body plethysmography was performed daily on five animals per group. Asterisks indicate differences from vehicle by two-way ANOVA with a Dunnett's multiple comparison test. (**E**) The histological features of acute lung injury (ALI) were blindly scored using an American Thoracic Society lung injury scoring system and a DAD scoring system. Three randomly chosen high-power (60×) fields of diseased lung were assessed per mouse. The numbers of mice scored per group: vehicle, $n = 7$; −2 hours, $n = 9$; +12 hours, $n = 9$; +24 hours, $n = 10$; +48 hours, $n = 9$. Asterisks indicate statistical significance compared to vehicle by Kruskal-Wallis with a Dunn's multiple comparison test. For all panels, the boxes encompass the 25th to 75th percentile, the line is at the median, and the whiskers represent the range. *, −2 and +12 hours compared to vehicle; **, +24 hours compared to vehicle; ***, +48 hours compared to vehicle.

Tukey's multiple comparison test, vehicle median = 3.4; −2 hours, median = 22.8, $P = 0.0035$; +12 hours, median = 20.0, $P = 0.0004$; Fig. 7J). Thus, about 20% of the mutations observed in the −2- and +12-hour groups resulted in a codon change and alteration of the nsp10 protein sequence. When extrapolating our results from nsp10 to the entirety of the 30-kb MERS-CoV genome, EIDD-2801 likely causes between 15 (+24-hour treatment) and 30 (−2-hour treatment) mutations per genome, 10 to 20% of which result in amino acid coding changes. Together, our data demonstrate that EIDD-2801–driven mutagenesis correlates well with the reductions in viral load, strongly suggestive of an error catastrophe–driven MOA under therapeutic conditions.

DISCUSSION

In the past 20 years, three novel human CoVs have emerged (*29*, *30*). The group 2b SARS-like CoV represent an existential and future threat to global health as evidenced by the emergence of SARS-CoV and SARS-CoV-2. Zoonotic SARS-like bat-CoV strains can use human angiotensin-converting enzyme 2 (ACE2) receptors, grow well in primary human airway cells, and vary by as much as 25% in key therapeutic and vaccine gene targets (*11*, *31*). Thus, to address the current public health emergency of COVID-19 and to maximize pandemic preparedness in the future, broad-based vaccines and therapeutics, which are active against the higher-risk RNA virus families prone to emergence, are desperately needed.

Small-molecule antivirals can exert their antiviral effect through multiple mechanisms including blocking viral entry, inhibiting a virally encoded enzyme, blocking virus particle formation, or targeting a host factor required for replication (*32*). Multiple direct acting antivirals are currently under evaluation in randomized control trials to treat COVID-19 including hydroxychloroquine, RDV, and lopinavir/ritonavir (*33*–*35*). Here, we report the broad-spectrum antiviral activity of NHC and its orally bioavailable prodrug EIDD-2801 against SARS-CoV, MERS-CoV, and the current pandemic strain SARS-CoV-2 in primary HAE cells. In addition to CoV, NHC is broadly active against multiple genetically distinct viruses including VEEV, influenzas A and B, Ebola, and Chikungunya viruses (*13*–*16*, *19*, *21*, *24*, *36*–*38*). Here, we show that prophylactic and therapeutic EIDD-2801 significantly reduced lung viral loads and

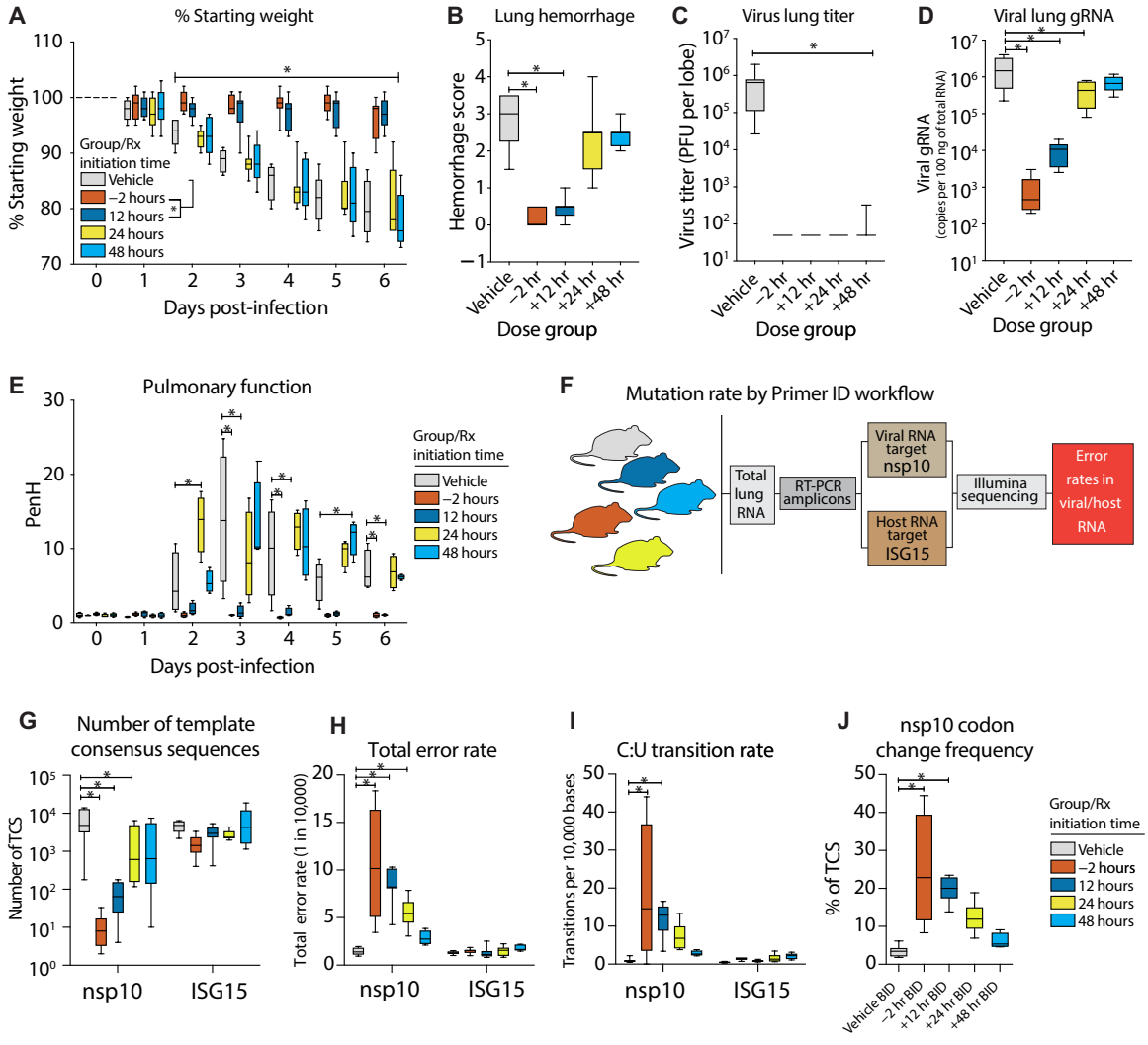

Fig. 7. Prophylactic and therapeutic EIDD-2801 reduces MERS-CoV replication and pathogenesis coincident with increased viral mutation rates. Equivalent numbers of 10- to 14-week-old male and female C57BL/6 hDPP4 mice were administered vehicle (10% PEG and 2.5% Cremophor RH 40 in water) or NHC prodrug EIDD-2801 beginning at −2, +12, +24, or +48 hpi and every 12 hours thereafter by oral gavage ($n = 10$ per group). Mice were intranasally infected with 5×10^4 PFU mouse-adapted MERS-CoV M35C4 strain. (**A**) Percent starting weight. Asterisks indicate differences between −2- and +12-hour group from vehicle by two-way ANOVA with Tukey's multiple comparison test. (**B**) Lung hemorrhage in mice from (A) scored on a scale of 0 to 4, where 0 is a normal pink healthy lung and 4 is a diffusely discolored dark red lung. (**C**) Virus lung titer in mice from (A) as determined by plaque assay. Asterisks in both (B) and (C) indicate differences from vehicle by Kruskal-Wallis with Dunn's multiple comparison test. (**D**) MERS-CoV genomic RNA in lung tissue by qRT-PCR. Asterisks indicate differences by one-way ANOVA with a Dunnett's multiple comparison test. (**E**) Pulmonary function by whole-body plethysmography was performed daily on four animals per group. Asterisks indicate differences from vehicle by two-way ANOVA with Tukey's multiple comparison test. (**F**) Workflow to measure mutation rate in MERS-CoV RNA and host transcript ISG15 by Primer ID in mouse lung tissue. (**G**) Number of template consensus sequences (TCSs) for MERS-CoV nsp10 and ISG15. (**H**) Total error rate in MERS-CoV nsp10 and ISG15. (**I**) Cytosine to uridine transition rate in MERS-CoV nsp10 and ISG15. In (G) to (I), asterisks indicate differences from vehicle by two-way ANOVA with Tukey's multiple comparison test. (**J**) Codon change frequency in MERS-CoV nsp10. Asterisks indicate differences from vehicle by Kruskal-Wallis with Dunn's multiple comparison test. For all panels, the boxes encompass the 25th to 75th percentile, the line is at the median, and the whiskers represent the range.

improved pulmonary function in mouse models of both SARS-CoV and MERS-CoV pathogenesis. Although the improvement in both SARS-CoV and MERS-CoV outcomes diminished with the delay of treatment initiation time, it is important to note that the kinetics of disease in mice are compressed as compared to that in humans. Whereas SARS-CoV and MERS-CoV lung titers peak on 1 to 2 dpi in mice concurrent with the onset of clinical signs and notable damage to the lung epithelium, in humans this occurs 7 to 10 days after the onset of symptoms (*19*, *28*, *39*, *40*). Thus, in mice, the window within which to treat emerging CoV infection before peak replication is compressed (e.g., 24 to 48 hours). As with oseltamivir treatment for influenza, which fails to provide a protective effect if administered >5 days after the onset of symptoms, the window in when to treat COVID-19 patients before peak virus replication is likely during the first week of symptoms when pharyngeal shedding is at its highest (*41*, *42*). However, virus replication and shedding may continue for several weeks in the most severe COVID-19 patients (*34*). Thus, early intervention with an antiviral-like EIDD-2801 is likely to provide

the most clinical benefit, although there may be opportunities in severe patients where the duration of virus replication may be extended. Our current study is clearly limited by the lack of in vivo efficacy testing with SARS-CoV-2. Currently, robust mouse models that recapitulate the SARS-CoV-2 pathogenesis observed in humans do not yet exist because of a noted virus spike glycoprotein and mouse ACE2 receptor incompatibility complicating the evaluation of medical countermeasures (*43*, *44*). In addition, SARS-CoV, MERS-CoV, and SARS-CoV-2 disease severity increases with increasing age. Our studies are limited by the lack of drug efficacy testing in CoV-aged mouse models that recapitulate the age-related increase in pathogenesis observed in humans (*45*). The data provided in this manuscript suggest that EIDD-2801 should be quickly evaluated in primate models of human disease using immediate models for MERS-CoV and SARS-CoV pathogenesis or newly described cynomolgus and rhesus macaque models for SARS-CoV-2 (*46*–*49*).

For VEEV and influenza, NHC/EIDD-2801 exerts its antiviral activity on the RdRp, leading to error catastrophe by inducing an error rate of replication that surpasses the error threshold allowed to sustain a virus population (*14*, *15*). This process occurs when NHC is incorporated during RNA synthesis and then subsequently misread, thus increasing mutation rates. Therefore, for CoV, the NHC MOA would appear less likely to be affected by the RNA proofreading activity encoded by the nsp14 exonuclease function that otherwise limits misincorporation (*50*). Here, we present data using Primer ID NGS to quantitate the frequency and identity of the mutational spectra in the MERS-CoV genome in both drug-treated primary human airway cells and in mice at single genome resolution. Because CoV are positive-sense RNA viruses that replicate through a negative-sense RNA intermediate, NHC incorporation as a C or a U can occur in both polarities of RNA. We found increased nucleotide transitions (A-to-G, G-to-A, C-to-U, and U-to-C) consistent with those reported after influenza and VEEV infections (*14*, *15*). Under identical conditions, RDV did not alter the mutation rate in MERS-CoV genomic RNA, supporting its reported MOA as a chain terminator of viral RNA synthesis (*26*). In primary human lung cell cultures and mice infected with MERS-CoV, the NHC mutation rates inversely correlated with a reduction in infectious virus. In addition, we found a positive correlation between increased mutation rates and the frequency of nonsynonymous mutations and the degree of therapeutic efficacy in mice. To explore the potential off-target effect in host mRNA, which may contribute to drug toxicity, we also examined the impact of NHC treatment on *ISG15* transcripts, a gene highly induced after MERS-CoV infection. Although ISG15 transcripts are present in great abundance, an accumulation of mutations was not observed in *ISG15* in this model even at 500 mg/kg dosing. These data also support previous studies using RNA-seq to demonstrate that the model CoV MHV displayed increased mutation frequencies after NHC treatment in vitro (*16*). With regard to nucleic acid specificity, ribonucleotides are efficiently removed from eukaryotic cell DNA; therefore, treating a viral infection with a mutagenic ribonucleoside analog should show a selectivity for incorporation into the viral genome and not be efficient at being incorporated into and inducing mutations into host cell DNA (*51*). Together, these data strongly support the notion that EIDD-2801 and its active nucleoside analog NHC exert their antiviral effect through the induction of error catastrophe in the targeted virus. While our data suggest that the MERS-CoV nsp14 proofreading activity appeared ineffective against NHC in vitro and EIDD-2801 in vivo, future studies should investigate the antiviral activity of NHC in the presence or absence of the nsp14 proofreading activity, as loss of this activity increased the sensitivity of MHV and SARS-CoV replication to RDV treatment (*50*). Together, our data support the continued development of EIDD-2801 as a potent broad-spectrum antiviral that could be useful in treating contemporary, newly emerged and emerging CoV infections of the future.

MATERIALS AND METHODS

Study design

The primary goal of this study was to determine the antiviral activity of the nucleoside analog NHC (EIDD-1931) against multiple emerging CoV in vitro and antiviral efficacy of its prodrug, EIDD-2801, in mouse models of CoV pathogenesis. In coupling cell lines and primary HAE cell cultures, we evaluated the antiviral activity of NHC against the three most recently emerged human CoV: SARS-CoV, MERS-CoV, and SARS-CoV-2. For both SARS-CoV and MERS-CoV, the data presented for HAE studies are representative of those from two to three separate human donors. For SARS-CoV-2, the HAE were from a single human donor. We evaluated drug cytotoxicity in both Calu-3 2B4 and HAE cell cultures. Calu-3 and the SARS-CoV and MERS-CoV HAE studies were performed in biological triplicate. HAE studies with SARS-CoV-2 and the SARS- and MERS-like bat-CoV were performed with two wells per condition. Drug effects were measured relative to vehicle controls in vitro, and comparisons in vivo were performed to vehicle controls. We also aimed to determine the antiviral efficacy of EIDD-2801 in mouse models of CoV pathogenesis. These studies were intended to provide the preclinical data to justify nonhuman primate studies and human clinical trials. Mice were age- and sex-matched and randomly assigned into groups before infection and treatment. Pathology was scored blinded by a board-certified veterinary pathologist. Primary data for all studies are provided in data file S1.

Ethics regulation of laboratory animals

Efficacy studies were performed in animal biosafety level 3 facilities at University of North Carolina (UNC) Chapel Hill. All work was conducted under protocols approved by the Institutional Animal Care and Use Committee (IACUC) at UNC Chapel Hill (Institutional Animal Care and Use Committee protocol no. 16-284) according to guidelines set by the Association for the Assessment and Accreditation of Laboratory Animal Care and the U.S. Department of Agriculture.

Compounds

The parental compound NHC (all in vitro studies) and its prodrug EIDD-2801 (all in vivo studies) were supplied by the EIDD. NHC was supplied as a 10 mM stock in dimethyl sulfoxide (DMSO) and EIDD-2801 as a solid and solubilized in vehicle containing 10% PEG-400 and 2.5% Cremophor RH 40 in water (10, 2.5, or 87.5%, all v/v) before use. RDV was solubilized in 100% DMSO and provided by Gilead Sciences Inc. as previously described (*18*, *19*).

Cell cultures

At UNC, the human lung epithelial cell line Calu-3 2B4 cells was maintained in Dulbecco's modified Eagle's medium (DMEM; Gibco), 20% fetal bovine serum (FBS; Hyclone), and 1× antibiotic/antimycotic (Gibco). At Vanderbilt University Medical Center (VUMC), Calu-3

2B4 cells were propagated in DMEM supplemented with 20% FBS (Gibco), penicillin and streptomycin (100 U/ml; Gibco), and 0.25 μM amphotericin B (Corning). At VUMC, Vero E6 cells were cultured in DMEM supplemented with 10% FBS (Gibco), 100 U/ml penicillin and streptomycin (Gibco), and 0.25 μM amphotericin B (Corning). At UNC, Vero E6 cells were cultured in DMEM supplemented with 10% FetalClone II (Hyclone) and 1× antibiotic/antimycotic (Gibco). Murine delayed brain tumor cells were maintained in DMEM supplemented with 10% FBS (Gibco), penicillin and streptomycin (100 U/ml; Gibco), and 0.25 μM amphotericin B (Corning). Primary HAE cell cultures were obtained from the Tissue Procurement and Cell Culture Core Laboratory in the Marsico Lung Institute/Cystic Fibrosis Research Center at UNC and are described more thoroughly below (*52*).

Virus strains

Except for SARS-CoV-2, all viruses used for these studies were derived from infectious clones and isolated as previously described (*53*). SARS-CoV-2 clinical isolate was obtained at VUMC and UNC from the U.S. Centers for Disease Control and Prevention (2019-nCoV/USA-WA1/2020 strain, GenBank accession no. MN985325.1) and passaged twice in Vero E6 cells at each respective institution to create a passage 5 working stock (*54*). Virus strains for in vitro experiments include SARS-CoV expressing the green fluorescent protein (GFP) in place of ORF7a/b (SARS-GFP) (*53*), bat spike receptor-binding domain (bat-SRBD) (*22*), a chimeric CoV strain derived from the HKU3 SARS-like bat-CoV genomic sequence that has the wild-type (Urbani SARS-CoV strain) RBD in the HKU3 spike gene to allow for virus replication in nonhuman primate cell lines and HAE cultures, SHC014 SARS-like bat-CoV (*11*), MERS-nLUC in the place of ORF3 (*19*), and MERS-CoV expressing the red fluorescent protein (RFP) gene in the place of ORF 5 (MERS-RFP) (*55*). The virus stock used for MERS-CoV in vivo studies was derived from a plaque-purified isolate of the mouse-adapted MERS-CoV p35C4 strain (*56*). The virus stock used for SARS-CoV in vivo studies was derived from the infectious clone of the mouse-adapted SARS-MA15 strain (*57*). All work with MHV was performed using the recombinant wild-type strain MHV-A59 (GenBank accession no. AY910861) (*58*).

In vitro antiviral activity experiments

MERS-nLUC in Calu-3

At 48 hours before infection, Calu-3 2B4 cells were plated in a 96-well black-walled clear bottom plate at 5×10^4 cells per well. A 10 mM stock of NHC was serially diluted in 100% DMSO in threefold increments to obtain a 10-point dilution series. MERS-nLUC was diluted in DMEM supplemented with 10% FBS and 1% antibiotic/antimycotic to achieve a multiplicity of infection (MOI) of 0.08. Cells were infected and concurrently treated with NHC in triplicate per drug dilution for 1 hour, after which viral inoculum was aspirated, cultures were rinsed once, and fresh medium containing drug or vehicle was added. At 48 hpi, nanoluciferase expression as a surrogate for virus replication was quantitated on a SpectraMax plate reader (Molecular Devices) according to the manufacturer's instructions (Promega, Nano-Glo). For the 100% inhibition control, diluted MERS-nLUC was exposed to short-wave ultraviolet light (UVP LLC) for 6 min to inhibit the ability of the virus to replicate. For the 0% inhibition control, cells were infected in the presence of vehicle only. DMSO was kept constant in all conditions at 0.05%. Values from triplicate wells per condition were averaged and compared to controls to generate a percent inhibition value for each drug dilution. The IC_{50} value was defined as the concentration at which there was a 50% decrease in luciferase expression. Data were analyzed using GraphPad Prism 8.0. The IC_{50} values were calculated by nonlinear regression analysis using the dose-response (variable slope) equation (four parameter logistic equation): $Y = \text{bottom} + (\text{top} - \text{bottom})/(1 + 10^{((\text{LogIC50} - X)*\text{HillSlope})})$. To measure cell viability to determine whether there was any NHC-induced cytotoxicity, Calu-3 2B4 cells were plated and treated with NHC only as described above. Cells were exposed to the same 10-point dilution series created for the in vitro efficacy studies. As above, 0.05% DMSO-treated cells served as the 0% cytotoxicity control. Wells without cells served as the 100% cytotoxic-positive control. After 48 hours, cell viability was measured on a SpectraMax (Molecular Devices) via CellTiter-Glo assay (Promega) according to the manufacturer's protocol. Similar data were obtained in three independent experiments.

SARS-CoV-2 in Calu-3

Calu-3 2B4 cells were adsorbed with an MOI of 0.1 PFU per cell of SARS-CoV-2 (2019-nCoV/USA-WA1/2020 strain) at 37°C. Plates were manually rocked every 10 min to redistribute the inoculum. After 30 min, virus inoculum was removed, cells were washed with phosphate-buffered saline (PBS) once to remove unbound virus, medium containing NHC or vehicle control (DMSO) was added back onto the cells, and cells were incubated for 72 hours at 37°C.

SARS-CoV-2 in Vero E6

Vero E6 cells were plated at 20,000 cells per well in a 96-well plate. Twenty-four hours later, medium containing a dose response of NHC was added concurrent with SARS-CoV-2 (2019-nCoV/USA-WA1/2020 strain) at an MOI of 0.05. At 48 hpi, cell viability was measured by CellTiter-Glo assay.

SARS-CoV, MERS-CoV, and SARS-CoV-2 in HAE

Human tracheobronchial epithelial cells provided by S. Randell were obtained from airway specimens resected from patients undergoing surgery under UNC Institutional Review Board–approved protocols (no. 03-1396) by the Cystic Fibrosis Center Tissue Culture Core. Primary cells were expanded to generate passage 1 cells, and passage 2 cells were plated at a density of 250,000 cells per well on Transwell-COL (12 mm in diameter) supports (Corning). HAE cultures were generated by provision of an air-liquid interface for 6 to 8 weeks to form well-differentiated, polarized cultures that resembled in vivo pseudostratified mucociliary epithelium (*59*)..At 48 hours before infection, the apical surface of the culture was washed with 500 μl of PBS for 1.5 hours at 37°C, and the cultures were moved into fresh air liquid interface media. Immediately before infection, apical surfaces were washed twice to remove accumulated mucus with 500 μl of PBS with each wash lasting 30 min at 37°C, and HAE cultures were moved into air liquid interface media containing various concentrations of NHC ranging from 10 to 0.0016 μM as indicated for each experiment (final % DMSO < 0.05%). Upon removing the second PBS wash, 200 μl of viral inoculum (SARS-GFP, MERS-RFP, or 2019-nCoV/USA-WA1/2020 strain) at an MOI of 0.5 was added to the apical surface, and HAE cultures were incubated for 2 hours at 37°C. Viral inoculum was then removed, and the apical surface of the cultures was washed three times with 500 μl of PBS and then incubated at 37°C until 48 hpi. For all HAE cultures, infectious virus produced was collected by washing the apical surface of the culture with 100 μl of PBS. Apical washes were stored at −80°C until analysis and titered by plaque assay as previously described (*19*).

qRT-PCR approach to assess cytotoxicity

Total RNA was isolated using the Zymo Direct-zol RNA MiniPrep Kit (Zymo Research) according to the manufacturer's directions. Cells were treated with 1 μM staurosporine (Sigma-Aldrich) as a positive control. First-strand complementary DNA (cDNA) was generated using SuperScript III Reverse Transcriptase (Life Technologies). For quantification of cellular markers of toxicity/apoptosis, real-time PCR was performed using commercially validated TaqMan-based primer-probe sets (table S1) and TaqMan Universal PCR Mix (Life Technologies). Results were then normalized as described above.

MERS-CoV genomic RNA qRT-PCR

Mouse lungs were stored in RNAlater (Thermo Fisher Scientific) at −80°C until processed via homogenization in TRIzol (Invitrogen). Total RNA was isolated using the Direct-zol RNA MiniPrep Kit (Zymo Research). Previously published TaqMan primers were synthesized by Integrated DNA Technologies (IDT) to quantify MERS genomic RNA [targeting orf1a: forward, 5′- GCACATCTGTGGTTCTCCTCTCT-3′; probe (6-FAM/ZEN/IBFQ), 5′- TGCTCCAACAGTTACAC-3′; reverse, 5′-AAGCCCAGGCCCTACTATTAGC-3′] (*60*). qRT-PCR was performed using 100 ng of total RNA compared to an RNA standard curve using TaqMan Fast Virus 1-Step Master Mix (Thermo Fisher Scientific) on a QuantStudio 3 (Applied Biosystems).

Quantification of SARS-CoV-2 viral RNA genome copy number by qRT-PCR

Cell supernatants were harvested in TRIzol LS reagent (Invitrogen), and RNA was purified after phase separation by chloroform as recommended by the manufacturer. The RNA in the aqueous phase was collected and further purified using the PureLink RNA Mini Kits (Invitrogen) according to the manufacturer's protocol. Viral RNA was quantified using one-step qRT-PCR on a StepOnePlus Real-Time PCR system (Applied Biosystems) by TaqMan Fast Virus 1-Step Master Mix chemistry (Applied Biosystems). SARS-CoV-2 N gene RNA was amplified using forward (5′-GACCCCAAAATCAGCGAAAT-3′) and reverse (5′-TCTGGTTACTGCCAGTTGAATCTG-3′) primers and probe (5′-FAM-ACCCCGCATTACGTTTGGTGGACC-BHQ1-3′) designed by the U.S. Centers for Disease Control and Prevention (oligonucleotides produced by IDT, catalog no. 10006606). Copy numbers were interpolated from a standard curve produced with dilutions of N gene RNA. In brief, SARS-CoV-2-N–positive control plasmid DNA (IDT, catalog no. 10006625) was amplified using forward (5′-TAATACGACTCACTATAGGGATGTCTGATAATGGACCCCA-3′) and reverse (5′- TTAGGCCTGAGTTGAGTCAG-3′) primers, resulting in a 1280 nucleotide fragment containing a T7 promoter. The PCR product was purified by column (Promega) and in vitro transcribed using the mMESSAGE mMACHINE T7 Transcription Kit (Invitrogen) according to the manufacturer's protocol. Transcribed RNA was purified using the RNeasy Mini Kit (Qiagen) according to the manufacturer's protocol, and serial 10-fold dilutions were quantified as described above.

Primer ID and deep sequencing

Primer ID NGS is designed to specifically identify and remove RT-PCR mutations while facilitating highly accurate sequence determination of single RNA molecules, because each cDNA is created with a barcoded degenerate primer (N10, 4^{10} combinations) from which Illumina-indexed libraries are made. We used a multiplexed Primer ID library prep approach and MiSeq sequencing to investigate the presence of mutations in the viral genomes and murine mRNA. We designed cDNA primers targeting multiple regions on the viral genome and murine mRNA, each with a block of random nucleotides (11-bp long) as the Primer ID (table S2) (*25*, *61*). Viral RNA was extracted using a QIAamp Viral RNA kit. A preamplification titration of templates was performed to estimate the amount of template to use. We used SuperScript III to make cDNA with multiplexed cDNA primers based on the regions to be sequenced. We used 41R_PID11 for the pilot sequencing and titration determination. For the MERS-CoV sequencing, we multiplexed nsp10_PID11, nsp12_PID11, and nsp14_PID11 for the cDNA reaction; for the murine mRNA sequencing, we used mixed primers of nsp10_PID11, ifit3_PID11, and isg15_PID11. After bead purification, we amplified the cDNA with a mixture of forward primers (based on the described schemes) and a universal reverse primer, followed by another round of PCR to incorporate Illumina sequencing adaptors and barcodes in the amplicons. After gel purification and quantification, we pooled 24 libraries for MiSeq 300-bp paired-end sequencing. The TCS pipeline version 1.38 (https://github.com/SwanstromLab/PID) was used to process the Primer ID sequencing data and construct TCSs to represent each individual input templates, and the sequences of each region in the pool were demultiplexed. The Ruby package viral_seq version 1.0.6 (https://rubygems.org/gems/viral_seq) was used to calculate the mutation rate at each position. National Center for Biotechnology Information (NCBI) sequence read archive (SRA) accession numbers for sequence data are as follows: PRJNA613261 (Fig. 5) and PRJNA613454 (Fig. 7).

In vivo experiments

We performed four mouse studies to evaluate the in vivo efficacy of the NHC prodrug (EIDD-2801). First, we performed prophylactic dose escalation studies for both SARS-CoV and MERS-CoV to determine the most efficacious dose of EIDD-2801 per virus. For SARS-CoV, in cohorts of equivalent numbers of male and female 20- to 29-week-old specific pathogen–free C57BL/6J (stock 000664, the Jackson laboratory) mice (n = 10 per dose group), we administered vehicle (10% PEG and 2.5% Cremophor RH 40 in water) or EIDD-2801 (50, 150, or 500 mg/kg) by oral gavage 2 hours before intranasal infection with 1×10^4 PFU mouse-adapted SARS-MA15 in 50 μl. Mice were anesthetized with a mixture of ketamine/xylazine before intranasal infection. Vehicle or drug was administered every 12 hours for the remainder of the study. Body weight and pulmonary function by WBP were measured daily. On 5 dpi, animals were sacrificed by isoflurane overdose, lungs were scored for lung hemorrhage, and the inferior right lobe was frozen at −80°C for viral titration via plaque assay. In brief, 500,000 Vero E6 cells per well were seeded in six-well plates. The following day, medium was removed, and serial dilutions of clarified lung homogenate were added per plate (10^{-1} to 10^{-6} dilutions) and incubated at 37°C for 1 hour, after which wells were overlaid with 1× DMEM, 5% FetalClone II Serum, 1× antibiotic/antimycotic, and 0.8% agarose. Two days after, plaques were enumerated to generate a plaque per milliliter value. Lung hemorrhage is a gross pathological phenotype readily observed by the naked eye driven by the degree of virus replication where the coloration of the lung changes from pink to dark red (*62*, *63*). The large left lobe was placed in 10% buffered formalin and stored at 4°C for 1 to 3 weeks until histological sectioning and analysis. For MERS-CoV, the prophylactic dose escalation studies were

performed similarly as done for SARS-CoV with our recently developed mouse model for MERS-CoV, which has an hDPP4 receptor (*28*). We performed all in vivo studies with EIDD-2801 in equivalent numbers of 10- to 14-week-old female and male C57BL/6J hDPP4 mice. Second, we intranasally infected mice with 5×10^4 PFU mouse-adapted MERS-CoV strain M35C4 in 50 μl. Third, to titer lungs by plaque assay, Vero CCL81 cells were used, and plaques were enumerated 3 dpi.

To determine the time at which therapeutic administration of EIDD-2801 would fail to improve outcomes with SARS-CoV or MERS-CoV infection, we performed therapeutic efficacy studies in mice where we initiated treatment 2 hours before infection or 12, 24, or 48 hpi. As 500 mg/kg provided the most complete protection from disease in prophylactic SARS-CoV studies, this dose was used for both therapeutic efficacy studies. Vehicle or EIDD-2801 was given via oral gavage twice daily after initiation of treatment. For both SARS-CoV and MERS-CoV, the infectious dose for the therapeutic studies and the mouse strains were the same as that used in the prophylactic studies. The numbers of mice per group for the SARS-CoV studies were as follows: vehicle ($n = 10$), −2 hours ($n = 10$), +12 hours ($n = 10$), +24 hours ($n = 10$), and +48 hours ($n = 10$). The numbers of mice per group for the MERS-CoV therapeutic studies were as follows: vehicle ($n = 9$), −2 hours ($n = 9$), +12 hours ($n = 9$), +24 hours ($n = 7$), and +48 hours ($n = 10$). As described above, each day mouse body weight and pulmonary function were quantitated. On 5 dpi for SARS-CoV and 6 dpi for MERS-CoV, animals were humanely euthanized, and tissues were harvested and analyzed as described above. In addition, for the MERS-CoV study, lung tissue was harvested and stored in RNAlater (Thermo Fisher Scientific) at −80°C, thawed, and homogenized in TRIzol reagent (Invitrogen), and total RNA was isolated using the Direct-zol RNA MiniPrep Kit (Zymo Research). This total RNA was then used for Primer ID and qRT-PCR.

Whole-body plethysmography

Pulmonary function was monitored once daily via WBP (Buxco respiratory solutions, DSI Inc.). Mice intended for this analysis were randomly chosen before the initiation of the study. In brief, after a 30-min acclimation time in the plethysmograph, data for 11 parameters were recorded every 2 s for 5 min.

ALI histological assessment tools

Two different and complementary quantitative histologic tools were used to determine whether antiviral treatments diminished the histopathologic features associated with lung injury. Both analyses and scoring were performed by a board-certified veterinary pathologist who was blinded to the treatment groups.

American Thoracic Society lung injury scoring tool

To help quantitate histological features of ALI observed in mouse models and increase their translation to the human condition, we used the American Thoracic Society scoring tool (*63*). In a blinded manner, we chose three random diseased fields of lung tissue at high power (60×), which were scored for the following: (A) neutrophils in the alveolar space (none, 0; one to five cells, 1; >5 cells, 2), (B) neutrophils in the interstitial space/septae (none, 0; one to five cells, 1; >5 cells, 2), (C) hyaline membranes (none, 0; one membrane, 1; >1 membrane, 2), (D) proteinaceous debris in air spaces (none, 0; one instance, 1; >1 instance, 2), and (E) alveolar septal thickening (<2× mock thickness, 0; 2 to 4× mock thickness, 1; >4× mock thickness, 2). To obtain a lung injury score per field, the scores for A to E were then put into the following formula, which contains multipliers that assign varying levels of importance for each phenotype of the disease state: score = $[(20 \times A) + (14 \times B) + (7 \times C) + (7 \times D) + (2 \times E)]/100$. The scores for the three fields per mouse were averaged to obtain a final score ranging from 0 to and including 1.

DAD tool

The second histological tool to quantitate lung injury was reported by Schmidt *et al.* (*64*). DAD is the pathological hallmark of ALI (*63*, *64*). Three random diseased fields of lung tissue were scored at high power (60×) for the following in a blinded manner: 1, absence of cellular sloughing and necrosis; 2, uncommon solitary cell sloughing and necrosis (one to two foci per field); 3, multifocal (3 + foci) cellular sloughing and necrosis with uncommon septal wall hyalinization; or 4, multifocal (>75% of field) cellular sloughing and necrosis with common and/or prominent hyaline membranes. The scores for the three fields per mouse were averaged to get a final DAD score per mouse.

nsp12 phylogenetic analysis and conservation modeling

CoV RdRp (nsp12) protein sequence alignments and phylogenetic trees were generated using Geneious Tree Builder in Geneious Prime (version 2020.0.5) and visualized using EvolView (www.evolgenius.info/evolview/). Protein similarity scores were calculated using BLOSUM62 matrix. The accession numbers used were as follows: PDCoV (KR265858), AIBV (NC_001451), HCoV-229E (JX503060), PEDV (NC_003436), MHV (AY700211), HCoV-HKU1 (DQ415904), HCoV-NL63 (JX504050), HCOV-OC43 (AY903460), HKU5-1 (NC_009020), MERS-CoV (JX869059), HKU9-4 (EF065516), 2019-nCoV (MN996528), HKU3-1 (DQ022305), SHC014 (KC881005), WIV1 (KF367457), and SARS-CoV (AY278741). Amino acid conservation scores of CoV RdRp were generated using ConSurf Server (https://consurf.tau.ac.il/) using the protein alignment described above and visualized on the SARS-CoV RdRp structure (Protein Data Bank: 6NUR) in PyMol (version 1.8.6.0) (*20*, *65*).

Statistical analysis

All statistical data analyses were performed in GraphPad Prism 8. Statistical significance for each end point was determined with specific statistical tests. In general, for metrics with multiple treatment groups with longitudinal data (e.g., mouse weight loss or pulmonary function over time), two-way ANOVA was performed with the suggested multiple comparison test as advised by Prism. For comparative data with for a single time point (e.g., lung titer), Kruskal-Wallis test or one-way ANOVA was performed with the suggested multiple comparison test. For each test, $P < 0.05$ was considered significant. Specific tests are noted in each figure legend.

SUPPLEMENTARY MATERIALS

stm.sciencemag.org/cgi/content/full/12/541/eabb5883/DC1

Fig. S1. Assessment of cytotoxicity of NHC in primary human epithelial cell cultures by qRT-PCR.

Fig. S2. High conservation of RdRp functional domains for SARS-CoV-2.

Fig. S3. Prophylactic EIDD-2801 reduces SARS-CoV replication and pathogenesis.

Fig. S4. Prophylactic EIDD-2801 reduces MERS-CoV replication and pathogenesis.

Table S1. Real-time PCR primer/probe sets for indicators of cellular apoptosis/toxicity.

Table S2. Primers used for MiSeq library prep and sequencing.

Data file S1. Primary data.

View/request a protocol for this paper from *Bio-protocol*.

REFERENCES AND NOTES

1. World Health Organization, "Middle East respiratory syndrome coronavirus (MERS-CoV)"; www.who.int/emergencies/mers-cov/en/.
2. E. de Wit, N. van Doremalen, D. Falzarano, V. J. Munster, SARS and MERS: Recent insights into emerging coronaviruses. *Nat. Rev. Microbiol.* **14**, 523–534 (2016).
3. D. Wang, B. Hu, C. Hu, F. Zhu, X. Liu, J. Zhang, B. Wang, H. Xiang, Z. Cheng, Y. Xiong, Y. Zhao, Y. Li, X. Wang, Z. Peng, Clinical characteristics of 138 hospitalized patients with 2019 novel coronavirus-infected pneumonia in Wuhan, China. *JAMA* **323**, 1061–1069 (2020).
4. S. J. Anthony, K. Gilardi, V. D. Menachery, T. Goldstein, B. Ssebide, R. Mbabazi, I. Navarrete-Macias, E. Liang, H. Wells, A. Hicks, A. Petrosov, D. K. Byarugaba, K. Debbink, K. H. Dinnon, T. Scobey, S. H. Randell, B. L. Yount, M. Cranfield, C. K. Johnson, R. S. Baric, W. I. Lipkin, J. A. K. Mazet, Further evidence for bats as the evolutionary source of Middle East respiratory syndrome coronavirus. *MBio* **8**, e00373-17 (2017).
5. B. Hu, X. Ge, L.-F. Wang, Z. Shi, Bat origin of human coronaviruses. *Virol. J.* **12**, 221 (2015).
6. J. Huynh, S. Li, B. Yount, A. Smith, L. Sturges, J. C. Olsen, J. Nagel, J. B. Johnson, S. Agnihothram, J. E. Gates, M. B. Frieman, R. S. Baric, E. F. Donaldson, Evidence supporting a zoonotic origin of human coronavirus strain NL63. *J. Virol.* **86**, 12816–12825 (2012).
7. A. M. Zaki, S. van Boheemen, T. M. Bestebroer, A. D. M. E. Osterhaus, R. A. M. Fouchier, Isolation of a novel coronavirus from a man with pneumonia in Saudi Arabia. *N. Engl. J. Med.* **367**, 1814–1820 (2012).
8. L.-Y. Hsu, C.-C. Lee, J. A. Green, B. Ang, N. I. Paton, L. Lee, J. S. Villacian, P.-L. Lim, A. Earnest, Y.-S. Leo, Severe acute respiratory syndrome (SARS) in Singapore: Clinical features of index patient and initial contacts. *Emerg. Infect. Dis.* **9**, 713–717 (2003).
9. P. Zhou, H. Fan, T. Lan, X.-L. Yang, W.-F. Shi, W. Zhang, Y. Zhu, Y.-W. Zhang, Q.-M. Xie, S. Mani, X.-S. Zheng, B. Li, J.-M. Li, H. Guo, G.-Q. Pei, X.-P. An, J.-W. Chen, L. Zhou, K.-J. Mai, Z.-X. Wu, D. Li, D. E. Anderson, L.-B. Zhang, S.-Y. Li, Z.-Q. Mi, T.-T. He, F. Cong, P.-J. Guo, R. Huang, Y. Luo, X.-L. Liu, J. Chen, Y. Huang, Q. Sun, X.-L.-L. Zhang, Y.-Y. Wang, S.-Z. Xing, Y.-S. Chen, Y. Sun, J. Li, P. Daszak, L.-F. Wang, Z.-L. Shi, Y.-G. Tong, J.-Y. Ma, Fatal swine acute diarrhoea syndrome caused by an HKU2-related coronavirus of bat origin. *Nature* **556**, 255–258 (2018).
10. P. C. Y. Woo, S. K. P. Lau, K. S. M. Li, R. W. S. Poon, B. H. L. Wong, H.-w. Tsoi, B. C. K. Yip, Y. Huang, K.-h. Chan, K.-y. Yuen, Molecular diversity of coronaviruses in bats. *Virology* **351**, 180–187 (2006).
11. V. D. Menachery, B. L. Yount Jr., K. Debbink, S. Agnihothram, L. E. Gralinski, J. A. Plante, R. L. Graham, T. Scobey, X.-Y. Ge, E. F. Donaldson, S. H. Randell, A. Lanzavecchia, W. A. Marasco, Z.-L. Shi, R. S. Baric, A SARS-like cluster of circulating bat coronaviruses shows potential for human emergence. *Nat. Med.* **21**, 1508–1513 (2015).
12. V. D. Menachery, B. L. Yount Jr., A. C. Sims, K. Debbink, S. S. Agnihothram, L. E. Gralinski, R. L. Graham, T. Scobey, J. A. Plante, S. R. Royal, J. Swanstrom, T. P. Sheahan, R. J. Pickles, D. Corti, S. H. Randell, A. Lanzavecchia, W. A. Marasco, R. S. Baric, SARS-like WIV1-CoV poised for human emergence. *Proc. Natl. Acad. Sci. U.S.A.* **113**, 3048–3053 (2016).
13. O. Reynard, X.-N. Nguyen, N. Alazard-Dany, V. Barateau, A. Cimarelli, V. E. Volchkov, Identification of a new ribonucleoside inhibitor of ebola virus replication. *Viruses* **7**, 6233–6240 (2015).
14. N. Urakova, V. Kuznetsova, D. K. Crossman, A. Sokratian, D. B. Guthrie, A. A. Kolykhalov, M. A. Lockwood, M. G. Natchus, M. R. Crowley, G. R. Painter, E. I. Frolova, I. Frolov, β-D-N^4-hydroxycytidine is a potent anti-alphavirus compound that induces a high level of mutations in the viral genome. *J. Virol.* **92**, e01965-17 (2018).
15. M. Toots, J.-J. Yoon, R. M. Cox, M. Hart, Z. M. Sticher, N. Makhsous, R. Plesker, A. H. Barrena, P. G. Reddy, D. G. Mitchell, R. C. Shean, G. R. Bluemling, A. A. Kolykhalov, A. L. Greninger, M. G. Natchus, G. R. Painter, R. K. Plemper, Characterization of orally efficacious influenza drug with high resistance barrier in ferrets and human airway epithelia. *Sci. Transl. Med.* **11**, eaax5866 (2019).
16. M. L. Agostini, A. J. Pruijssers, J. D. Chappell, J. Gribble, X. Lu, E. L. Andres, G. R. Bluemling, M. A. Lockwood, T. P. Sheahan, A. C. Sims, M. G. Natchus, M. Saindane, A. A. Kolykhalov, G. R. Painter, R. S. Baric, M. R. Denison, Small-molecule antiviral β-D-N^4-hydroxycytidine inhibits a proofreading-intact coronavirus with a high genetic barrier to resistance. *J. Virol.* **93**, e01348-19 (2019).
17. P. C. Jordan, C. Liu, P. Raynaud, M. K. Lo, C. F. Spiropoulou, J. A. Symons, L. Beigelman, J. Deval, Initiation, extension, and termination of RNA synthesis by a paramyxovirus polymerase. *PLOS Pathog.* **14**, e1006889 (2018).
18. T. P. Sheahan, A. C. Sims, S. R. Leist, A. Schäfer, J. Won, A. J. Brown, S. A. Montgomery, A. Hogg, D. Babusis, M. O. Clarke, J. E. Spahn, L. Bauer, S. Sellers, D. Porter, J. Y. Feng, T. Cihlar, R. Jordan, M. R. Denison, R. S. Baric, Comparative therapeutic efficacy of remdesivir and combination lopinavir, ritonavir, and interferon beta against MERS-CoV. *Nat. Commun.* **11**, 222 (2020).
19. T. P. Sheahan, A. C. Sims, R. L. Graham, V. D. Menachery, L. E. Gralinski, J. B. Case, S. R. Leist, K. Pyrc, J. Y. Feng, I. Trantcheva, R. Bannister, Y. Park, D. Babusis, M. O. Clarke, R. L. Mackman, J. E. Spahn, C. A. Palmiotti, D. Siegel, A. S. Ray, T. Cihlar, R. Jordan, M. R. Denison, R. S. Baric, Broad-spectrum antiviral GS-5734 inhibits both epidemic and zoonotic coronaviruses. *Sci. Transl. Med.* **9**, eaal3653 (2017).
20. R. N. Kirchdoerfer, A. B. Ward, Structure of the SARS-CoV nsp12 polymerase bound to nsp7 and nsp8 co-factors. *Nat. Commun.* **10**, 2342 (2019).
21. M. L. Agostini, E. L. Andres, A. C. Sims, R. L. Graham, T. P. Sheahan, X. Lu, E. C. Smith, J. B. Case, J. Y. Feng, R. Jordan, A. S. Ray, T. Cihlar, D. Siegel, R. L. Mackman, M. O. Clarke, R. S. Baric, M. R. Denison, Coronavirus susceptibility to the antiviral remdesivir (GS-5734) is mediated by the viral polymerase and the proofreading exoribonuclease. *MBio* **9**, e00221-18 (2018).
22. M. M. Becker, R. L. Graham, E. F. Donaldson, B. Rockx, A. C. Sims, T. Sheahan, R. J. Pickles, D. Corti, R. E. Johnston, R. S. Baric, M. R. Denison, Synthetic recombinant bat SARS-like coronavirus is infectious in cultured cells and in mice. *Proc. Natl. Acad. Sci. U.S.A.* **105**, 19944–19949 (2008).
23. S. Agnihothram, B. L. Yount Jr., E. F. Donaldson, J. Huynh, V. D. Menachery, L. E. Gralinski, R. L. Graham, M. M. Becker, S. Tomar, T. D. Scobey, H. L. Osswald, A. Whitmore, R. Gopal, A. K. Ghosh, A. Mesecar, M. Zambon, M. Heise, M. R. Denison, R. S. Baric, A mouse model for *Betacoronavirus* subgroup 2c using a bat coronavirus strain HKU5 variant. *MBio* **5**, e00047-14 (2014).
24. J.-J. Yoon, M. Toots, S. Lee, M.-E. Lee, B. Ludeke, J. M. Luczo, K. Ganti, R. M. Cox, Z. M. Sticher, V. Edpuganti, D. G. Mitchell, M. A. Lockwood, A. A. Kolykhalov, A. L. Greninger, M. L. Moore, G. R. Painter, A. C. Lowen, S. M. Tompkins, R. Fearns, M. G. Natchus, R. K. Plemper, Orally efficacious broad-spectrum ribonucleoside analog inhibitor of influenza and respiratory syncytial viruses. *Antimicrob. Agents Chemother.* **62**, e00766-18 (2018).
25. S. Zhou, C. Jones, P. Mieczkowski, R. Swanstrom, Primer ID validates template sampling depth and greatly reduces the error rate of next-generation sequencing of HIV-1 genomic RNA Populations. *J. Virol.* **89**, 8540–8555 (2015).
26. E. P. Tchesnokov, J. Y. Feng, D. P. Porter, M. Götte, Mechanism of inhibition of Ebola virus RNA-dependent RNA polymerase by remdesivir. *Viruses* **11**, E326 (2019).
27. V. D. Menachery, L. E. Gralinski, R. S. Baric, M. T. Ferris, New metrics for evaluating viral respiratory pathogenesis. *PLOS ONE* **10**, e0131451 (2015).
28. A. S. Cockrell, B. L. Yount, T. Scobey, K. Jensen, M. Douglas, A. Beall, X.-C. Tang, W. A. Marasco, M. T. Heise, R. S. Baric, A mouse model for MERS coronavirus-induced acute respiratory distress syndrome. *Nat. Microbiol.* **2**, 16226 (2016).
29. H. D. Marston, G. K. Folkers, D. M. Morens, A. S. Fauci, Emerging viral diseases: Confronting threats with new technologies. *Sci. Transl. Med.* **6**, 253ps10 (2014).
30. C. I. Paules, H. D. Marston, A. S. Fauci, Coronavirus infections—More than just the common cold. *JAMA* **323**, 707–708 (2020).
31. A. J. Brown, J. J. Won, R. L. Graham, K. H. Dinnon III, A. C. Sims, J. Y. Feng, T. Cihlar, M. R. Denison, R. S. Baric, T. P. Sheahan, Broad spectrum antiviral remdesivir inhibits human endemic and zoonotic deltacoronaviruses with a highly divergent RNA dependent RNA polymerase. *Antivir. Res.* **169**, 104541 (2019).
32. A. Zumla, J. F. W. Chan, E. I. Azhar, D. S. C. Hui, K.-Y. Yuen, Coronaviruses – drug discovery and therapeutic options. *Nat. Rev. Drug Discov.* **15**, 327–347 (2016).
33. A. Cortegiani, G. Ingoglia, M. Ippolito, A. Giarratano, S. Einav, A systematic review on the efficacy and safety of chloroquine for the treatment of COVID-19. *J. Crit. Care*, S0883-9441(20)30390-7 (2020).
34. F. X. Lescure, L. Bouadma, D. Nguyen, M. Parisey, P. H. Wicky, S. Behillil, A. Gaymard, M. Bouscambert-Duchamp, F. Donati, Q. Le Hingrat, V. Enouf, N. Houhou-Fidouh, M. Valette, A. Mailles, J. C. Lucet, F. Mentre, X. Duval, D. Descamps, D. Malvy, J. F. Timsit, B. Lina, S. van der Werf, Y. Yazdanpanah, Clinical and virological data of the first cases of COVID-19 in Europe: A case series. *Lancet Infect. Dis.*, S1473-3099(20)30200-0 (2020).
35. B. Cao, Y. Wang, D. Wen, W. Liu, J. Wang, G. Fan, L. Ruan, B. Song, Y. Cai, M. Wei, X. Li, J. Xia, N. Chen, J. Xiang, T. Yu, T. Bai, X. Xie, L. Zhang, C. Li, Y. Yuan, H. Chen, H. Li, H. Huang, S. Tu, F. Gong, Y. Liu, Y. Wei, C. Dong, F. Zhou, X. Gu, J. Xu, Z. Liu, Y. Zhang, H. Li, L. Shang, K. Wang, K. Li, X. Zhou, X. Dong, Z. Qu, S. Lu, X. Hu, S. Ruan, S. Luo, J. Wu, L. Peng, F. Cheng, L. Pan, J. Zou, C. Jia, J. Wang, X. Liu, S. Wang, X. Wu, Q. Ge, J. He, H. Zhan, F. Qiu, L. Guo, C. Huang, T. Jaki, F. G. Hayden, P. W. Horby, D. Zhang, C. Wang, A trial of lopinavir–ritonavir in adults hospitalized with severe covid-19. *N. Engl. J. Med.*, 10.1056/NEJMoa2001282, (2020).
36. M. Ehteshami, S. Tao, K. Zandi, H.-M. Hsiao, Y. Jiang, E. Hammond, F. Amblard, O. O. Russell, A. Merits, R. F. Schinazi, Characterization of β-D-N^4-hydroxycytidine as a novel inhibitor of chikungunya virus. *Antimicrob. Agents Chemother.* **61**, e02395-16 (2017).
37. T. K. Warren, R. Jordan, M. K. Lo, A. S. Ray, R. L. Mackman, V. Soloveva, D. Siegel, M. Perron, R. Bannister, H. C. Hui, N. Larson, R. Strickley, J. Wells, K. S. Stuthman, S. A. Van Tongeren, N. L. Garza, G. Donnelly, A. C. Shurtleff, C. J. Retterer, D. Gharaibeh, R. Zamani, T. Kenny, B. P. Eaton, E. Grimes, L. S. Welch, L. Gomba, C. L. Wilhelmsen, D. K. Nichols, J. E. Nuss, E. R. Nagle, J. R. Kugelman, G. Palacios, E. Doerffler, S. Neville, E. Carra, M. O. Clarke, L. Zhang, W. Lew, B. Ross, Q. Wang, K. Chun, L. Wolfe, D. Babusis, Y. Park, K. M. Stray, I. Trancheva, J. Y. Feng, O. Barauskas, Y. Xu, P. Wong, M. R. Braun, M. Flint, L. K. McMullan, S. S. Chen, R. Fearns, S. Swaminathan, D. L. Mayers, C. F. Spiropoulou, W. A. Lee,

S. T. Nichol, T. Cihlar, S. Bavari, Therapeutic efficacy of the small molecule GS-5734 against Ebola virus in rhesus monkeys. *Nature* **531**, 381–385 (2016).
38. M. K. Lo, R. Jordan, A. Arvey, J. Sudhamsu, P. Shrivastava-Ranjan, A. L. Hotard, M. Flint, L. K. McMullan, D. Siegel, M. O. Clarke, R. L. Mackman, H. C. Hui, M. Perron, A. S. Ray, T. Cihlar, S. T. Nichol, C. F. Spiropoulou, GS-5734 and its parent nucleoside analog inhibit Filo-, Pneumo-, and Paramyxoviruses. *Sci. Rep.* **7**, 43395 (2017).
39. M. D. Oh, W. B. Park, P. G. Choe, S. J. Choi, J. I. Kim, J. Chae, S. S. Park, E. C. Kim, H. S. Oh, E. J. Kim, E. Y. Nam, S. H. Na, D. K. Kim, S. M. Lee, K. H. Song, J. H. Bang, E. S. Kim, H. B. Kim, S. W. Park, N. J. Kim, Viral load kinetics of MERS coronavirus infection. *N. Engl. J. Med.* **375**, 1303–1305 (2016).
40. J. S. Peiris, C. M. Chu, V. C. Cheng, K. S. Chan, I. F. Hung, L. L. Poon, K. I. Law, B. S. Tang, T. Y. Hon, C. S. Chan, K. H. Chan, J. S. Ng, B. J. Zheng, W. L. Ng, R. W. Lai, Y. Guan, K. Y. Yuen; HKU/UCH SARS Study Group, Clinical progression and viral load in a community outbreak of coronavirus-associated SARS pneumonia: A prospective study. *Lancet* **361**, 1767–1772 (2003).
41. R. Wölfel, V. M. Corman, W. Guggemos, M. Seilmaier, S. Zange, M. A. Müller, D. Niemeyer, T. C. Jones, P. Vollmar, C. Rothe, M. Hoelscher, T. Bleicker, S. Brünink, J. Schneider, R. Ehmann, K. Zwirglmaier, C. Drosten, C. Wendtner, Virological assessment of hospitalized patients with COVID-2019. *Nature*, 10.1038/s41586-020-2196-x (2020).
42. H. Yu, Z. Feng, T. M. Uyeki, Q. Liao, L. Zhou, L. Feng, M. Ye, N. Xiang, Y. Huai, Y. Yuan, H. Jiang, Y. Zheng, P. Gargiullo, Z. Peng, Y. Feng, J. Zheng, C. Xu, Y. Zhang, Y. Shu, Z. Gao, W. Yang, Y. Wang, Risk factors for severe illness with 2009 pandemic influenza A (H1N1) virus infection in China. *Clin. Infect. Dis.* **52**, 457–465 (2011).
43. Y. Wan, J. Shang, R. Graham, R. S. Baric, F. Li, Receptor recognition by novel coronavirus from Wuhan: An analysis based on decade-long structural studies of SARS. *J. Virology* **94**, e00127-20 (2020).
44. P. Zhou, X.-L. Yang, X.-G. Wang, B. Hu, L. Zhang, W. Zhang, H.-R. Si, Y. Zhu, B. Li, C.-L. Huang, H.-D. Chen, J. Chen, Y. Luo, H. Guo, R.-D. Jiang, M.-Q. Liu, Y. Chen, X.-R. Shen, X. Wang, X.-S. Zheng, K. Zhao, Q.-J. Chen, F. Deng, L.-L. Liu, B. Yan, F.-X. Zhan, Y.-Y. Wang, G. Xiao, Z.-L. Shi, Discovery of a novel coronavirus associated with the recent pneumonia outbreak in humans and its potential bat origin. *bioRxiv*, 2020.01.22.914952 (2020).
45. T. Sheahan, A. Whitmore, K. Long, M. Ferris, B. Rockx, W. Funkhouser, E. Donaldson, L. Gralinski, M. Collier, M. Heise, N. Davis, R. Johnston, R. S. Baric, Successful vaccination strategies that protect aged mice from lethal challenge from influenza virus and heterologous severe acute respiratory syndrome coronavirus. *J. Virol.* **85**, 217–230 (2011).
46. E. de Wit, A. L. Rasmussen, D. Falzarano, T. Bushmaker, F. Feldmann, D. L. Brining, E. R. Fischer, C. Martellaro, A. Okumura, J. Chang, D. Scott, A. G. Benecke, M. G. Katze, H. Feldmann, V. J. Munster, Middle East respiratory syndrome coronavirus (MERS-CoV) causes transient lower respiratory tract infection in rhesus macaques. *Proc. Natl. Acad. Sci. U.S.A.* **110**, 16598–16603 (2013).
47. J. McAuliffe, L. Vogel, A. Roberts, G. Fahle, S. Fischer, W. J. Shieh, E. Butler, S. Zaki, M. St. Claire, B. Murphy, K. Subbarao, Replication of SARS coronavirus administered into the respiratory tract of African Green, rhesus and cynomolgus monkeys. *Virology* **330**, 8–15 (2004).
48. V. J. Munster, F. Feldmann, B. N. Williamson, N. van Doremalen, L. Pérez-Pérez, J. Schulz, K. Meade-White, A. Okumura, J. Callison, B. Brumbaugh, V. A. Avanzato, R. Rosenke, P. W. Hanley, G. Saturday, D. Scott, E. R. Fischer, E. de Wit, Respiratory disease and virus shedding in rhesus macaques inoculated with SARS-CoV-2. *bioRxiv*, 2020.03.21.001628 (2020).
49. B. Rockx, T. Kuiken, S. Herfst, T. Bestebroer, M. M. Lamers, D. de Meulder, G. van Amerongen, J. van den Brand, N. M. A. Okba, D. Schipper, P. van Run, L. Leijten, E. Verschoor, B. Verstrepen, J. Langermans, C. Drosten, M. F. van Vlissingen, R. Fouchier, R. de Swart, M. Koopmans, B. L. Haagmans, Comparative pathogenesis of COVID-19, MERS And SARS in a non-human primate model. *bioRxiv*, 2020.03.17.995639 (2020).
50. E. C. Smith, H. Blanc, M. C. Surdel, M. Vignuzzi, M. R. Denison, Coronaviruses lacking exoribonuclease activity are susceptible to lethal mutagenesis: Evidence for proofreading and potential therapeutics. *PLOS Pathog.* **9**, e1003565 (2013).
51. T. Suzuki, K. Moriyama, C. Otsuka, D. Loakes, K. Negishi, Template properties of mutagenic cytosine analogues in reverse transcription. *Nucleic Acids Res.* **34**, 6438–6449 (2006).
52. M. L. Fulcher, S. H. Randell, Human nasal and tracheo-bronchial respiratory epithelial cell culture. *Methods Mol. Biol.* **945**, 109–121 (2013).
53. A. C. Sims, R. S. Baric, B. Yount, S. E. Burkett, P. L. Collins, R. J. Pickles, Severe acute respiratory syndrome coronavirus infection of human ciliated airway epithelia: Role of ciliated cells in viral spread in the conducting airways of the lungs. *J. Virol.* **79**, 15511–15524 (2005).
54. J. Harcourt, A. Tamin, X. Lu, S. Kamili, S. K. Sakthivel, J. Murray, K. Queen, Y. Tao, C. R. Paden, J. Zhang, Y. Li, A. Uehara, H. Wang, C. Goldsmith, H. A. Bullock, L. Wang, B. Whitaker, B. Lynch, R. Gautam, C. Schindewolf, K. G. Lokugamage, D. Scharton, J. A. Plante, D. Mirchandani, S. G. Widen, K. Narayanan, S. Makino, T. G. Ksiazek, K. S. Plante, S. C. Weaver, S. Lindstrom, S. Tong, V. D. Menachery, N. J. Thornburg, Severe acute respiratory syndrome coronavirus 2 from patient with 2019 novel coronavirus disease, United States. *Emerg. Infect. Dis.* **26**, 10.3201/eid2606.200516 (2020).
55. T. Scobey, B. L. Yount, A. C. Sims, E. F. Donaldson, S. S. Agnihothram, V. D. Menachery, R. L. Graham, J. Swanstrom, P. F. Bove, J. D. Kim, S. Grego, S. H. Randell, R. S. Baric, Reverse genetics with a full-length infectious cDNA of the Middle East respiratory syndrome coronavirus. *Proc. Natl. Acad. Sci. U.S.A.* **110**, 16157–16162 (2013).
56. M. G. Douglas, J. F. Kocher, T. Scobey, R. S. Baric, A. S. Cockrell, Adaptive evolution influences the infectious dose of MERS-CoV necessary to achieve severe respiratory disease. *Virology* **517**, 98–107 (2018).
57. A. Roberts, D. Deming, C. D. Paddock, A. Cheng, B. Yount, L. Vogel, B. D. Herman, T. Sheahan, M. Heise, G. L. Genrich, S. R. Zaki, R. Baric, K. Subbarao, A mouse-adapted SARS-coronavirus causes disease and mortality in BALB/c mice. *PLOS Pathog.* **3**, e5 (2007).
58. B. Yount, M. R. Denison, S. R. Weiss, R. S. Baric, Systematic assembly of a full-length infectious cDNA of mouse hepatitis virus strain A59. *J. Virol.* **76**, 11065–11078 (2002).
59. M. L. Fulcher, S. Gabriel, K. A. Burns, J. R. Yankaskas, S. H. Randell, Well-differentiated human airway epithelial cell cultures. *Methods Mol. Med.* **107**, 183–206 (2005).
60. F. Almazan, M. L. DeDiego, I. Sola, S. Zuñiga, J. L. Nieto-Torres, S. Marquez-Jurado, G. Andrés, L. Enjuanes, Engineering a replication-competent, propagation-defective Middle East respiratory syndrome coronavirus as a vaccine candidate. *MBio* **4**, e00650-13 (2013).
61. C. B. Jabara, C. D. Jones, J. Roach, J. A. Anderson, R. Swanstrom, Accurate sampling and deep sequencing of the HIV-1 protease gene using a Primer ID. *Proc. Natl. Acad. Sci. U.S.A.* **108**, 20166–20171 (2011).
62. M. Fukushi, T. Ito, T. Oka, T. Kitazawa, T. Miyoshi-Akiyama, T. Kirikae, M. Yamashita, K. Kudo, Serial histopathological examination of the lungs of mice infected with influenza A virus PR8 strain. *PLOS ONE* **6**, e21207 (2011).
63. G. Matute-Bello, G. Downey, B. B. Moore, S. D. Groshong, M. A. Matthay, A. S. Slutsky, W. M. Kuebler; Acute Lung Injury in Animals Study Group, An official American Thoracic Society workshop report: Features and measurements of experimental acute lung injury in animals. *Am. J. Respir. Cell Mol. Biol.* **44**, 725–738 (2011).
64. M. E. Schmidt, C. J. Knudson, S. M. Hartwig, L. L. Pewe, D. K. Meyerholz, R. A. Langlois, J. T. Harty, S. M. Varga, Memory CD8 T cells mediate severe immunopathology following respiratory syncytial virus infection. *PLOS Pathog.* **14**, e1006810 (2018).
65. H. Ashkenazy, S. Abadi, E. Martz, O. Chay, I. Mayrose, T. Pupko, N. Ben-Tal, ConSurf 2016: An improved methodology to estimate and visualize evolutionary conservation in macromolecules. *Nucleic Acids Res.* **44**, W344–W350 (2016).

Funding: We would like to acknowledge the following funding sources: Antiviral Drug Discovery and Development Center (5U19AI109680 and 1U19AI142759) awarded to M.D. and R.S.B., a partnership grant from the National Institutes of Allergy and Infectious Disease (NIAID; 5R01AI132178) awarded to T.P.S. and R.S.B., and an NIAID R01 grant (AI108197) awarded to M.D. and R.S.B. NIAID contract (HHSN272201500008C) was awarded to G.P., and The Emory Institute for Drug Development and a subcontract from this was awarded to R.S.B. and M.R.D. M.L.A. was funded through training grants F31AI133952 and T32AI112541. The Marsico Lung Institute Tissue Procurement and Cell Culture Core is supported by NIH grant DK065988 and Cystic Fibrosis Foundation grant BOUCHE15RO. **Author contributions:** A.C.S., T.P.S., A.J.P., and M.L.A. designed in vitro efficacy studies. A.C.S., A.J.B., T.P.S., R.L.G., A.J.P., L.J.S., and M.L.A. executed and/or analyzed in vitro efficacy studies. X.L., T.M.H., and A.S.G. designed, optimized, and/or executed the SARS-CoV-2 qRT-PCR studies. J.H., A.T., and N.J.T. provided the clinical isolate of SARS-CoV-2. T.P.S., A.A.K., M.G.N., G.P., and R.S.B. designed in vivo efficacy studies. T.P.S., A.C.S., S.Z., C.S.H., and R.S. designed, executed, and/or analyzed the Primer ID NGS data. K.H.D. performed structural modeling and phylogenetics and sequence alignments. M.L.A., A.J.P., J.D.C., and M.R.D. designed, performed, and/or executed the construction of RDV resistant MHV and performed cross-resistance studies. T.P.S., A.S., and S.R.L. executed and analyzed in vivo efficacy studies. A.S. and S.R.L. performed whole body plethysmography for in vivo studies. S.A.M. assessed all lung pathology. G.R.B. and M.S. were responsible for synthesis and scale-up of small molecules. T.P.S., A.C.S., S.Z., S.R.L, A.S., K.H.D., M.L.A., A.J.P., J.D.C, G.R.B., A.A.K., G.P., R.S., M.R.D., and R.S.B. wrote the manuscript. The findings and conclusions in this report are those of the author(s) and do not necessarily represent the official position of the U.S. Centers for Disease Control and Prevention. Names of specific vendors, manufacturers, or products are included for public health and informational purposes; inclusion does not imply endorsement of the vendors, manufacturers, or products by the U.S. Centers for Disease Control and Prevention or the U.S. Department of Health and Human Services. **Competing interests:** UNC is pursuing intellectual property (IP) protection for Primer ID, and R.S. has received nominal royalties. G.R.R, M.G.N., and G.R.P hold patents 62096915, 62201140, 2015066144, 62306163, 2017021759, 16083177, 62595907, 62626998, 62760434,

2018064503, 62971559, and 62988133, "N4-hydroxycytidine and derivatives and anti-viral uses related thereto," relating to this work. This study could affect their personal financial status. **Data and materials availability:** All data associated with this study are present in the paper or the Supplementary Materials. Sequence data are deposited to NCBI SRA as PRJNA613261 and PRJNA613454.

Submitted 5 March 2020
Accepted 3 April 2020
Published 29 April 2020
10.1126/scitranslmed.abb5883

Citation: T. P. Sheahan, A. C. Sims, S. Zhou, R. L. Graham, A. J. Pruijssers, M. L. Agostini, S. R. Leist, A. Schäfer, K. H. Dinnon III, L. J. Stevens, J. D. Chappell, X. Lu, T. M. Hughes, A. S. George, C. S. Hill, S. A. Montgomery, A. J. Brown, G. R. Bluemling, M. G. Natchus, M. Saindane, A. A. Kolykhalov, G. Painter, J. Harcourt, A. Tamin, N. J. Thornburg, R. Swanstrom, M. R. Denison, R. S. Baric, An orally bioavailable broad-spectrum antiviral inhibits SARS-CoV-2 in human airway epithelial cell cultures and multiple coronaviruses in mice. *Sci. Transl. Med.* **12**, eabb5883 (2020).

Science Translational Medicine

An orally bioavailable broad-spectrum antiviral inhibits SARS-CoV-2 in human airway epithelial cell cultures and multiple coronaviruses in mice

Timothy P. Sheahan, Amy C. Sims, Shuntai Zhou, Rachel L. Graham, Andrea J. Pruijssers, Maria L. Agostini, Sarah R. Leist, Alexandra Schäfer, Kenneth H. Dinnon III, Laura J. Stevens, James D. Chappell, Xiaotao Lu, Tia M. Hughes, Amelia S. George, Collin S. Hill, Stephanie A. Montgomery, Ariane J. Brown, Gregory R. Bluemling, Michael G. Natchus, Manohar Saindane, Alexander A. Kolykhalov, George Painter, Jennifer Harcourt, Azaibi Tamin, Natalie J. Thornburg, Ronald Swanstrom, Mark R. Denison and Ralph S. Baric

Sci Transl Med **12**, eabb5883.
First published 6 April 2020
DOI: 10.1126/scitranslmed.abb5883

Catastrophic consequences

Broad-spectrum antivirals are desirable, particularly in the context of emerging zoonotic infections for which specific interventions do not yet exist. Sheahan *et al.* tested the potential of a ribonucleoside analog previously shown to be active against other RNA viruses such as influenza and Ebola virus to combat coronaviruses. This drug was effective in cell lines and primary human airway epithelial cultures against multiple coronaviruses including SARS-CoV-2. Mouse models of SARS and MERS demonstrated that early treatment reduced viral replication and damage to the lungs. Mechanistically, this drug is incorporated into the viral RNA, inducing mutations and eventually leading to error catastrophe in the virus. In this manner, inducing catastrophe could help avoid catastrophe by stemming the next pandemic.

Science Translational Medicine (ISSN 1946-6242) is published by the American Association for the Advancement of Science, 1200 New York Avenue NW, Washington, DC 20005. The title *Science Translational Medicine* is a registered trademark of AAAS.